

Review

# Low-Dimensional Nanostructured Photocatalysts for Efficient CO<sub>2</sub> Conversion into Solar Fuels

Hossam A. E. Omr <sup>1,2</sup>, Mark W. Horn <sup>3</sup> and Hyeonseok Lee <sup>1,\*</sup>

<sup>1</sup> Department of Photonics, National Sun Yat-sen University, No. 70, Lien-Hai Rd, Kaohsiung 80424, Taiwan; hossamaeo1@gmail.com

<sup>2</sup> Department of Chemistry, Faculty of Science, Assiut University, Assiut 71516, Egypt

<sup>3</sup> Department of Engineering Science and Mechanics, Pennsylvania State University, University Park, PA 16802, USA; mhorn@engr.psu.edu

\* Correspondence: hslee611@mail.nsysu.edu.tw

**Abstract:** The ongoing energy crisis and global warming caused by the massive usage of fossil fuels and emission of CO<sub>2</sub> into atmosphere continue to motivate researchers to investigate possible solutions. The conversion of CO<sub>2</sub> into value-added solar fuels by photocatalysts has been suggested as an intriguing solution to simultaneously mitigate global warming and provide a source of energy in an environmentally friendly manner. There has been considerable effort for nearly four decades investigating the performance of CO<sub>2</sub> conversion by photocatalysts, much of which has focused on structure or materials modification. In particular, the application of low-dimensional structures for photocatalysts is a promising pathway. Depending on the materials and fabrication methods, low-dimensional nanomaterials can be formed in zero dimensional structures such as quantum dots, one-dimensional structures such as nanowires, nanotubes, nanobelts, and nanorods, and two-dimensional structures such as nanosheets and thin films. These nanostructures increase the effective surface area and possess unique electrical and optical properties, including the quantum confinement effect in semiconductors or the localized surface plasmon resonance effect in noble metals at the nanoscale. These unique properties can play a vital role in enhancing the performance of photocatalytic CO<sub>2</sub> conversion into solar fuels by engineering the nanostructures. In this review, we provide an overview of photocatalytic CO<sub>2</sub> conversion and especially focus on nanostructured photocatalysts. The fundamental mechanism of photocatalytic CO<sub>2</sub> conversion is discussed and recent progresses of low-dimensional photocatalysts for efficient conversion of CO<sub>2</sub> into solar fuels are presented.

**Keywords:** photocatalysis; carbon dioxide conversion; nanostructures; low-dimensional photocatalysts; solar fuels



**Citation:** Omr, H.A.E.; Horn, M.W.; Lee, H. Low-Dimensional Nanostructured Photocatalysts for Efficient CO<sub>2</sub> Conversion into Solar Fuels. *Catalysts* **2021**, *11*, 418. <https://doi.org/10.3390/catal11040418>

Academic Editor: Ewa Kowalska

Received: 24 February 2021

Accepted: 24 March 2021

Published: 25 March 2021

**Publisher's Note:** MDPI stays neutral with regard to jurisdictional claims in published maps and institutional affiliations.



**Copyright:** © 2021 by the authors. Licensee MDPI, Basel, Switzerland. This article is an open access article distributed under the terms and conditions of the Creative Commons Attribution (CC BY) license (<https://creativecommons.org/licenses/by/4.0/>).

## 1. Introduction

The fast-developing modern technology and explosive world population growth have resulted in a huge demand for and consumption of energy. According to an investigation from the U.S. Energy Information Administration, more than 600 quadrillion Btus of energy were spent in 2020 and it is expected that the demand will continue to skyrocket annually. To meet this huge energy demand every year, energy production has been predominately dependent on fossil fuels such as coal, oil, or natural gas. The energy production by fossil fuels is inextricably linked to the gigantic CO<sub>2</sub> emission of more than 30 billion metric tons every year and, in turn, the accumulated CO<sub>2</sub> in our atmosphere is deemed to be the main cause of many environmental problems such as global warming and erratic weather patterns. In this context, there is great motivation to find a way of reducing atmospheric CO<sub>2</sub> and producing energy at the same time. For these problems, CO<sub>2</sub> conversion by photocatalyst materials under light illumination could be an expedient solution. This is because natural sunlight provides clean, renewable, and abundant energy,

and photocatalysts can be activated by light energy from the Sun, while simultaneously consuming CO<sub>2</sub> for energy production.

In 1978, by Halmann [1], the first demonstration of the photocatalytic conversion of CO<sub>2</sub> in aqueous solution into liquid fuels such as methanol, formic acid, and formaldehyde was achieved over p-type gallium phosphide semiconductor. The same year, the photoartificial synthesis by SrTiO<sub>3</sub> photocatalysts for CH<sub>4</sub> production through the gas-solid phase reaction of CO<sub>2</sub> and H<sub>2</sub>O was reported by Hemminger [2]. In 1979, another pioneering work by Fujishima and his coworkers introduced the artificial synthesis of solar fuels from a CO<sub>2</sub>-saturated electrolyte under light illumination. In this study, liquid CO<sub>2</sub> was converted with various semiconductor photocatalysts such as TiO<sub>2</sub>, ZnO, CdS, GaP, SiC, and WO<sub>3</sub> to produce methane, methanol, formaldehyde and formic acid [3]. Since these historical works mentioned above, several semiconductor materials have been investigated for the conversion of CO<sub>2</sub> into useful fuels, including graphitic carbon nitride (g-C<sub>3</sub>N<sub>4</sub>), graphene, conjugated polymers, covalent organic framework, metal organic frameworks, metal chalcogenides, metal oxides, black phosphorus, bismuth-based materials, and perovskites [4–14]. Moreover, a variety of strategies and approaches have been applied to improve the photocatalyst performance through elemental doping, solid solution, heterostructure, nanostructuralization, surface engineering and modification, crystal facet engineering, cocatalysts utilization, or dimensionality tailoring [15–19].

Of the strategies researched to boost the efficiency of CO<sub>2</sub> conversion, decreasing the dimensionality and constructing nanostructures of the photocatalyst have attracted a lot of attention owing to their favorable advantages in photocatalysis: first, nanostructured photocatalysts suppress the carrier recombination due to their higher crystallinity compared to non-nanostructured materials [20–22]; second, the implementation of low dimensionality modifies the electronic structure of bulk materials due to the quantum confinement effect in semiconductors or localized surface plasmon resonance effect in noble metals at the nanoscale; third, low-dimensional materials possess larger surface-area-to-volume ratio in comparison with bulk materials, providing more reaction sites. All three features can contribute to improved solar-driven catalytic reactions [19,23].

In this review, we summarize the fundamental knowledge about CO<sub>2</sub> conversion into useful fuels by photocatalysts and offer insights on the pivotal role of low dimensional structure in photocatalysts for efficient conversion of CO<sub>2</sub> into chemical fuels such as CO, CH<sub>4</sub>, CH<sub>3</sub>OH, and C<sub>2</sub>H<sub>5</sub>OH that are useful sources of energy. We highlight the recent developments of low-dimensional nanostructures for photocatalysts toward chemical fuels production via the photoreduction of CO<sub>2</sub>. Finally, we provide the strategies to enhance the performance of CO<sub>2</sub> conversion over low-dimensionally nanostructured photocatalysts.

## 2. The Main Fundamentals of CO<sub>2</sub> Photoconversion into Solar Fuels and Hydrocarbon Species

### 2.1. Nature of CO<sub>2</sub>

Carbon dioxide (CO<sub>2</sub>) is one of the primary greenhouse gases but, at the same time, it is the main resource for solar fuel production when coupled with proton donors such as H<sub>2</sub>O for photocatalytic CO<sub>2</sub> conversion. Hence, understanding the nature of the gaseous CO<sub>2</sub> molecule itself is necessary for efficient utilization of photocatalysts. CO<sub>2</sub> is a stable linear molecule among carbon compounds because of it is in the highest oxidation state of carbon, C<sup>+4</sup> [19]. The CO<sub>2</sub> molecule has two C=O bonds with a dissociation energy of ~750 kJ/mol, which is quite larger than those in other chemical bonds such as C-H (~430 kJ/mol) and C-C (~336 kJ/mol). For this reason, the reduction of CO<sub>2</sub> to produce solar fuels requires additional energy to break the C=O bond and form, for example, a C-H bond [24]. Owing to its stability and strong bonding, photocatalytic reduction of CO<sub>2</sub> into solar fuels can be achieved primarily with the support of proton donors such as H<sub>2</sub>O or H<sub>2</sub> [25].

## 2.2. CO<sub>2</sub> Adsorption on the Surface of Photocatalysts

The adsorption and activation of CO<sub>2</sub> on a solid surface is one of the essential steps in achieving CO<sub>2</sub> reduction and photocatalytic performance. The adsorption mechanism of CO<sub>2</sub> on several semiconductor photocatalysts has been investigated [26,27]. For instance, the adsorption of CO<sub>2</sub> on TiO<sub>2</sub> surface has been investigated by Minot and coworkers [26]. Various adsorption modes of CO<sub>2</sub> over a rutile TiO<sub>2</sub> surface have been studied using first-principles calculations. The oxygen atom of CO<sub>2</sub> molecules favors the interaction with the acidic titanium cation over the surface forming a Ti–OCO bond [26]. The adsorption of CO<sub>2</sub> on a photocatalyst surface includes the interaction between the CO<sub>2</sub> molecule and the surface atoms of the photocatalyst. This adsorption may occur with a charge transfer from the photocatalyst to the linear and stable CO<sub>2</sub> molecule which can induce the formation of partially charged and bent adsorbate, CO<sub>2</sub><sup>δ-,-</sup>, and this adsorbate can form three different molecular structures, as shown in Figure 1: oxygen coordination, carbon coordination, and mixed coordination [24,28,29]. The beneficial feature of CO<sub>2</sub><sup>δ-,-</sup>, is that it has decrease in the lowest unoccupied molecular orbital (LUMO) of the CO<sub>2</sub> energy level as linear CO<sub>2</sub> molecule transformed into the bent structure. This would facilitate the charge transfer between a photocatalyst and CO<sub>2</sub><sup>δ-,-</sup>, [24,28,29].

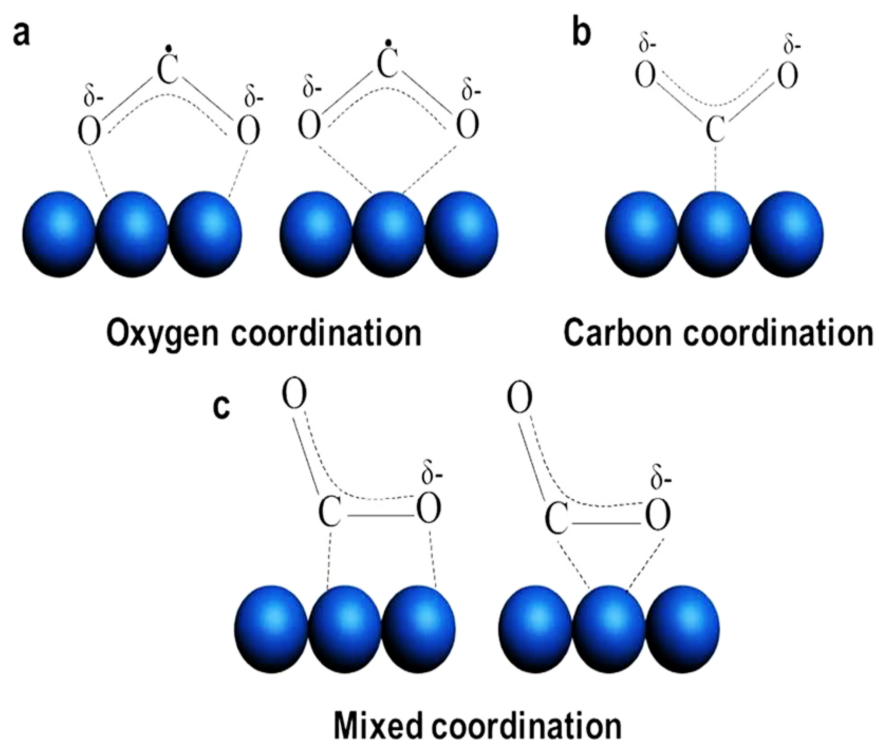


**Figure 1.** Schematic illustration of the different types of CO<sub>2</sub> adsorption modes (Adapted from [24]).

In the photocatalytic reaction, the photocatalyst donates electron to the adsorbed species on the surface to initiate the reduction process of CO<sub>2</sub> in the presence of protons. As shown in Table 1, the solar fuel production is determined by the number of electrons and protons included in the reaction [20,24]. For example, two electrons are required for CO evolution, while methane production is an eight-electron reaction. The adsorption of CO<sub>2</sub> on the photocatalyst surface can be improved by a variety of strategies. First, decreasing the structural dimensionality of photocatalyst can improve the surface area of the photocatalyst to allow more adsorption. Second, enhanced density of active sites by incorporation of surface defects, such as oxygen and sulfur vacancies, can improve the CO<sub>2</sub> adsorption. Third, utilization of noble metal nanoparticles can help improve the adsorption due to lowered activation energy of the CO<sub>2</sub> reduction [24,30].

**Table 1.** Standard electrochemical potentials of CO<sub>2</sub> and H<sub>2</sub>O at 25 °C and atmospheric pressure [20,24].

	Reaction	E° at pH 7 (V vs. NHE)	Solar Fuel
CO <sub>2</sub> reduction	CO <sub>2</sub> + 2H <sup>+</sup> + 2e <sup>-</sup> → CO + H <sub>2</sub> O	-0.51	CO
	CO <sub>2</sub> + 8H <sup>+</sup> + 8e <sup>-</sup> → CH <sub>4</sub> + 2H <sub>2</sub> O	-0.24	CH <sub>4</sub>
	CO <sub>2</sub> + 6H <sup>+</sup> + 6e <sup>-</sup> → CH <sub>3</sub> OH + H <sub>2</sub> O	-0.39	CH <sub>3</sub> OH
	2CO <sub>2</sub> + 12H <sup>+</sup> + 12e <sup>-</sup> → C <sub>2</sub> H <sub>5</sub> OH + 3H <sub>2</sub> O	-0.33	C <sub>2</sub> H <sub>5</sub> OH
	CO <sub>2</sub> + 2H <sup>+</sup> + 2e <sup>-</sup> → HCOOH	-0.58	HCOOH
H <sub>2</sub> O oxidation	CO <sub>2</sub> + 4H <sup>+</sup> + 4e <sup>-</sup> → HCHO + H <sub>2</sub> O	-0.48	HCHO
	2H <sub>2</sub> O → O <sub>2</sub> + 4H <sup>+</sup>	+0.81	O <sub>2</sub>

### 2.3. The Mechanism of Efficient CO<sub>2</sub> Photoconversion

Upon absorption of light over the photocatalyst, charge carrier pairs are generated to achieve the photosynthesis of solar fuels accompanying the water splitting as shown in Table 1. To execute the conversion of CO<sub>2</sub> into useful fuels from the thermodynamic point of view, the conduction band minimum (CBM), and the valence band maximum (VBM) of a photocatalyst should bracket the redox potential of CO<sub>2</sub> and the oxidation potential of water, respectively, as shown in Table 1 and Figure 3. As results of the reactions, various solar fuels can be formed dependent on the number of electrons and protons in the presence of CO<sub>2</sub> and water under the illumination.

The artificial photosynthesis of solar fuels using semiconductor photocatalysts consists of three essential steps, as described in Figure 2. Firstly, incident photons of light with energy higher than that of semiconductor band gap ( $E_g$ ) induce the generation of the electron-hole pairs (Process (i)). Secondly, the photogenerated charge carriers are transferred to the photocatalyst surface (Process (ii)). Thirdly, the electrons and holes react on the surface of photocatalyst with CO<sub>2</sub> and H<sub>2</sub>O for evolution of solar fuels (Process (iii)). For efficient photocatalytic conversion of CO<sub>2</sub> into fuels, the ideal semiconductor photocatalyst should have optimized band gap for efficient light harvesting and photocarrier generation, facile charge separation and transportation, vigorously activated sites and high surface area for maximum adsorption of CO<sub>2</sub> and water [30,31].

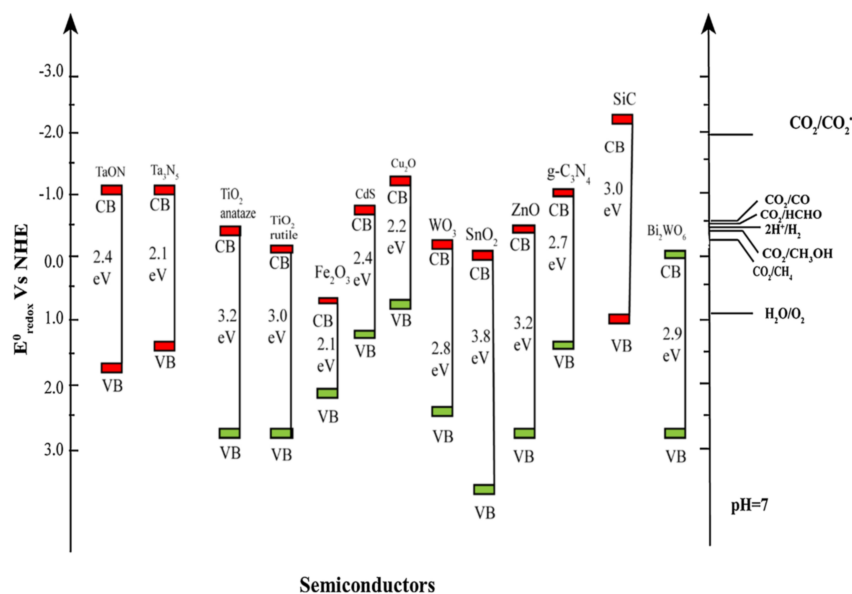


**Figure 2.** A schematic diagram of CO<sub>2</sub> photocatalytic conversion process over photocatalyst. Process (i): light absorption and generation of photocarriers via a semiconductor photocatalyst. Process (ii): charge carrier separation and transfer to the surface of photocatalyst. Process (iii): reactions of CO<sub>2</sub> and H<sub>2</sub>O with electrons and holes, respectively to produce solar fuels.

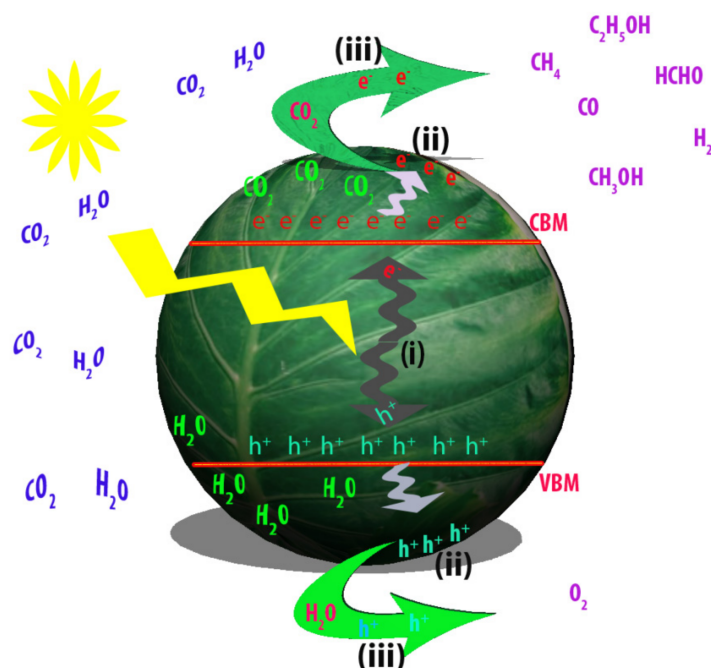


**Figure 3.** The energy band structures of semiconductor photocatalysts and the corresponding redox potentials of CO<sub>2</sub> reduction into solar fuels (Adapted from [32]).

### 3. State-of-the-Art Progress in Low-Dimensional Nanostructured Photocatalyst

Low-dimensional materials are defined as nanostructured materials characterized by sizes smaller than 100 nm in at least one dimension. Low-dimensional materials include insulators, semiconductors, and metals [33]. In terms of their morphologies, the low-dimensional materials can be classified into three categories as can be seen in Figure 4. First, zero-dimensional materials such as nanoparticles, nanosphere, and quantum dots (QDs). Second, one-dimensional materials including nanowires (NWs), nanotubes (NTs), nanobelts (NBs), nanorods (NRs), and nanoribbons. Third, two-dimensional materials which includes nanosheets and thin film [23,34]. Low-dimensional semiconductor materials are widely used for efficient artificial synthesis of solar fuels and constructed with various materials such as titanium dioxide [21], carbon [35], phosphorus [36], transition metal dichalcogenides [37], group IV monochalcogenides (MX, M=Sn, Si, Ge, and X=S, Se) [38], conjugated polymers [39], and perovskite [40]. In this section, we introduce the important features of low-dimensional photocatalytic materials and recent advances of low-dimensional nanostructured photocatalysts related to CO<sub>2</sub> conversion into solar fuels.

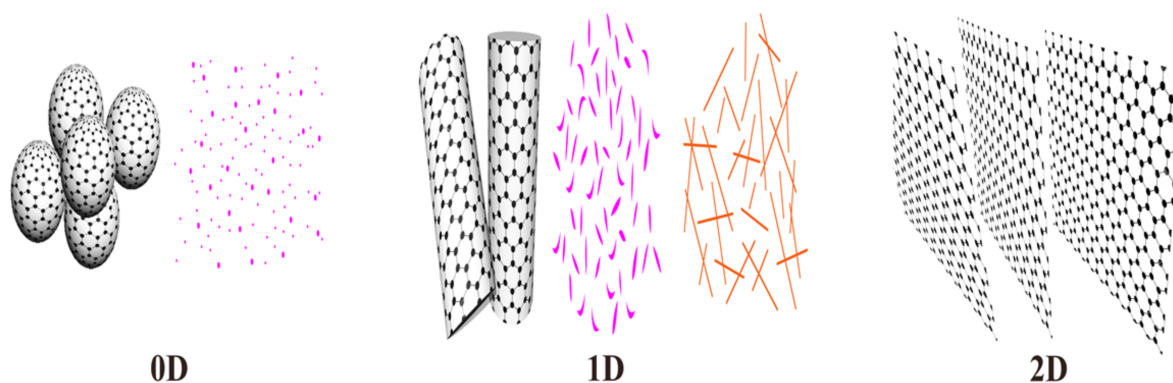


**Figure 4.** Classification of low-dimensional materials based on the morphology into two dimensional (2D), one dimensional (1D), and zero dimensional (0D) nanomaterials.

### 3.1. Low-Dimensional Semiconductor Materials in Photocatalytic Application

Low-dimensional semiconductor materials possess unique optical and electronic properties which are distinct from those of their bulk counterparts. The motion of electrons in low-dimensional materials is confined by their nanostructures, which is known as quantum confinement effect [41]. The quantum confinement results in the unique properties of the low-dimensional nanomaterials that would benefit the performance of photocatalysts.

In general, the optical properties of low-dimensional semiconductor materials are affected by this quantum confinement. Osterloh et al. [42] reported that the optical and photocatalytic properties of CdSe nanocrystals can be tuned by the quantum confinement effect. CdSe QDs of diameter ranged between 1.8 and 6 nm were fabricated by a facile aqueous method using 2-mercaptoethanol as a surface capping agent and 2-propanol as precipitating agent. The decrease in the size of CdSe QDs is accompanied with widening of optical band gap, which is directly related to the efficient utilization of the photocatalyst [42]. In addition, the quantum confinement effect has influence on the electrical properties of the semiconductors such as modulation of the potential energies of conduction and valence bands. In general, the electronic band structure of low-dimensional materials varies with dimensionality as a result of the different distribution of densities of state. The dimensional reduction of semiconductors is accompanied with energy discontinuity compared to 3D materials. Namely, the density of states (DOS) of 3D materials are distributed in  $E^{1/2}$  in terms of energy,  $E$  while there is a step-like DOS distribution in 2D materials. The DOS for quantum wires is proportional to  $E^{-1/2}$ . Once the electron is confined in all directions as in quantum dots, the density of states become series of  $\delta$ -peak functions and exists only at discrete energies [34]. In addition, reducing the dimensionality of the semiconductor photocatalyst could contribute to increase in DOS. Xie and coworkers fabricated ultrathin TiO<sub>2</sub> flakes via sonication of lamellar TiO<sub>2</sub>-octylamine. It is reported that the transformation of 3D TiO<sub>2</sub> into ultrathin TiO<sub>2</sub> flakes facilitate the transfer of the photoexcited electron into the conduction band of TiO<sub>2</sub>. They observed an increased DOS at the edge of band, suggesting enhanced electrical properties of TiO<sub>2</sub> materials [43].

These unique electronic properties of low-dimensional materials also benefit the CO<sub>2</sub> conversion performance of photocatalysts. TiO<sub>2</sub> nanosheets of 1.66-nm thickness reported by Xie and coworkers exhibited formate production rate of 1.9  $\mu\text{mol}\cdot\text{g}^{-1}\cdot\text{h}^{-1}$  and this conversion rate is 450 times higher than that by bulk TiO<sub>2</sub> [43]. Chen and coworkers have functionalized graphene QDs by addition of 1,1'-bi(2-naphthylamine) to coal graphene QDs followed by solvothermal reaction at 180 °C to form C=N bonds [11]. The as-synthesized graphene QD displayed outstanding activity of 0.695  $\mu\text{mol}\cdot\text{g}^{-1}\cdot\text{h}^{-1}$  toward CO<sub>2</sub> conversion into methanol under visible light radiation, which is three times higher than that of coal graphene QDs. In addition, the band gap of functionalized graphene QDs has been engineered for modulation of valence band maximum and conduction band minimum which can control the photocatalyst selectivity toward the desired product [11]. Recently, Gong and coauthors reported the confinement effect in low-dimensional C<sub>3</sub>N<sub>4</sub>/CdSe photocatalyst through the photocatalytic conversion of CO<sub>2</sub> into methanol. Herein, CdSe QDs with 1.2–4.1 nm of diameters were synthesized using 2-mercaptopropionic acid and 2-propanol as surface-passivating and size-selective precipitating agents, respectively. The CdSe QD was loaded on polymeric C<sub>3</sub>N<sub>4</sub> using an impregnation method. It was found that the CdSe QDs with 2.2 nm particle size achieved 73% of selectivity and 186.4  $\mu\text{mol}\cdot\text{g}^{-1}\cdot\text{h}^{-1}$  of methanol production. The methanol activity and selectivity were enhanced by virtue of tuning the conduction band potential [44].

We have discussed some general features of low-dimensional photocatalyst above. Hereafter, we focus more specifically on research in terms of dimensions and introduce more literature reviews on low-dimensional photocatalytic application. Table 2 summaries various low-dimensional photocatalysts that have been introduced including the examples following.

**Table 2.** Summary of low-dimensional photocatalysts used in photocatalytic reduction of CO<sub>2</sub> into solar fuels. NC: Nanocrystal, GQD: Graphene Quantum Dot, NF: Nanofiber, NS: Nanosheet, CNT: carbon nanotube, Mt: montmorillonite, m-CN: modified g-C<sub>3</sub>N<sub>4</sub>, NR: nanorod, NW: nanowire, CND: carbon nano dot, p-CN: protonated g-C<sub>3</sub>N<sub>4</sub>, PGCN: porous g-C<sub>3</sub>N<sub>4</sub>, TEOA: triethanolamine, bpy: bipyridine, C<sub>3</sub>N<sub>4</sub>: Melon-based polymeric carbon nitride, UTNS: ultrathin nanosheet, P-g-C<sub>3</sub>N<sub>4</sub>: Phosphorus doped g-C<sub>3</sub>N<sub>4</sub>.

Dimensionality	Morphology	Photocatalyst	Light Source	Reducing Agent	Main Product	Activity [ $\mu\text{mol}\cdot\text{g}^{-1}\cdot\text{h}^{-1}$ ]	Ref.
0D	QD 3–12 nm	CsPbBr <sub>3</sub>	300 W Xe lamp	H <sub>2</sub> O	CO CH <sub>4</sub>	4.26 1.53	[45]
	QD 2.3 nm	Cs <sub>3</sub> Bi <sub>2</sub> I <sub>9</sub>	300 W Xe lamp	H <sub>2</sub> O	CO	1.15	
	QD 2.9 nm	Cs <sub>3</sub> Bi <sub>2</sub> Br <sub>9</sub>	300 W Xe lamp	H <sub>2</sub> O	CO	26.95	[46]
	QD 2.4 nm	Cs <sub>3</sub> Bi <sub>2</sub> Cl <sub>9</sub>	300 W Xe lamp	H <sub>2</sub> O	CO	21.01	
	NC 9.5 nm	Cs <sub>2</sub> AgBiBr <sub>6</sub>	AM 1.5G	Ethyl acetate	CO CH <sub>4</sub>	2.35 1.6	[47]
	QD 9.45 nm	FAPbBr <sub>3</sub>	300 W Xe arc lamp	H <sub>2</sub> O	CO CH <sub>4</sub>	181.25 16.9	[48]
	QD 5.86 nm	GQD	300 W Xe lamp 420 nm cutoff filter	H <sub>2</sub> O	CH <sub>3</sub> OH	0.695	[11]
1D	NR	CeO <sub>2</sub>	300 W Xe lamp	H <sub>2</sub> O	CO	0.020	[49]
	NT	TiO <sub>2</sub>	300 W Xe arc lamp 320 nm < $\lambda$ < 780 nm	H <sub>2</sub> O	CH <sub>4</sub>	2.128	[21]
	NR	TiO <sub>2</sub>	300 W Xe arc lamp 320 nm < $\lambda$ < 780 nm	H <sub>2</sub> O	CH <sub>4</sub>	1.41	[21]
	NT	P-g-C <sub>3</sub> N <sub>4</sub>	300 W Xe lamp	H <sub>2</sub> O/TEOA	CO CH <sub>4</sub>	2.37 1.81	[50]
	NT	PGCN	300 W Xe lamp	H <sub>2</sub> O/MeCN /TEOA	CO	103.6	[51]
	NT	Bi <sub>12</sub> O <sub>17</sub> Cl <sub>2</sub>	300 W Xe lamp	H <sub>2</sub> O	CO	48.6	[52]
	NT	Bi <sub>12</sub> O <sub>17</sub> Br <sub>2</sub>	300 W Xe lamp	H <sub>2</sub> O	CO	34.5	[53]
2D	NS	g-C <sub>3</sub> N <sub>4</sub>	300 W Xe arc lamp	MeCN/TEOA (4:1)	CO CH <sub>4</sub>	5.407 1.549	[54]
	UTNS	g-C <sub>3</sub> N <sub>4</sub>	300 W Xe lamp	H <sub>2</sub> O	CH <sub>4</sub> CH <sub>3</sub> OH	1.39 1.87	[55]
	UTNS	SiC	300 W Xe lamp	H <sub>2</sub> O	CO CH <sub>4</sub>	1.29 3.11	[56]
	UTNS	Bi <sub>2</sub> MoO <sub>6</sub>	300 W Xe lamp	H <sub>2</sub> O	CO	3.62	[57]
0D/1D	QD/NW	Black P/WO <sub>3</sub>	300 W Xenon arc lamp	H <sub>2</sub> O	CO C <sub>2</sub> H <sub>4</sub>	~ 135 ~ 11	[13]
	QD (10 nm)/NT	WS <sub>2</sub> /Bi <sub>2</sub> S <sub>3</sub>	300 W Xe arc lamp	H <sub>2</sub> O	CH <sub>3</sub> OH C <sub>2</sub> H <sub>5</sub> OH	9.55 6.95	[58]
	QD (3.5 nm)/NW	Ti <sub>3</sub> C <sub>2</sub> /Cu <sub>2</sub> O	300 W Xe lamp	H <sub>2</sub> O	CH <sub>3</sub> OH	78.50	[59]
0D/2D	QD (1.6 nm)/NS	CuO/WO <sub>3</sub>	300 W Xe lamp $\lambda > 400$ nm	H <sub>2</sub> O	CO	1.58	[60]
	ND (4.4 nm)/NS	CND/p-CN	Xe arc lamp	H <sub>2</sub> O	CO CH <sub>4</sub>	5.88 2.92	[61]
	QD/NS	TiO <sub>2</sub> /g-C <sub>3</sub> N <sub>4</sub>	300 W Xe lamp $\lambda > 400$ nm	MeCN/TEOA	CO	77.8	[62]
	QD (5nm)/NS	Au/TiO <sub>2</sub>	300 W Xe arc lamp	H <sub>2</sub> O	CO CH <sub>4</sub>	19.75 70.34	[63]
	QD (7nm) /NS	CsPbBr <sub>3</sub> /Bi <sub>2</sub> WO <sub>6</sub>	300 W Xe lamp $\lambda > 400$ nm	H <sub>2</sub> O	CO/CH <sub>4</sub>	503 $\mu\text{mol}\cdot\text{g}^{-1}$	[64]

Table 2. Cont.

Dimensionality	Morphology	Photocatalyst	Light Source	Reducing Agent	Main Product	Activity [ $\mu\text{mol}\cdot\text{g}^{-1}\cdot\text{h}^{-1}$ ]	Ref.
1D/2D	NF/NS	TiO <sub>2</sub> /MoS <sub>2</sub>	350 W Xe lamp	H <sub>2</sub> O	CH <sub>4</sub> CH <sub>3</sub> OH	2.86 2.55	[65]
	NT/NS	CNT/g-C <sub>3</sub> N <sub>4</sub>	200 W Hg and solar simulator	H <sub>2</sub> O	CO CH <sub>4</sub>	410 74	[66]
	NR/NS/NF	Au/TiO <sub>2</sub> /BiVO <sub>4</sub>	300 W Xe lamp	H <sub>2</sub> O	CO CH <sub>4</sub>	2.5 7.5	[67]
2D/2D	NS/NS	Ti <sub>3</sub> C <sub>2</sub> /Bi <sub>2</sub> WO <sub>6</sub>	300 W Xe lamp	H <sub>2</sub> O	CH <sub>4</sub> CH <sub>3</sub> OH	1.78 0.44	[68]
	NS/NS	Bi <sub>2</sub> WO <sub>6</sub> /BiOI	500 W Xe arc lamp $\lambda < 400$ nm	H <sub>2</sub> O	CH <sub>4</sub>	2.92	[69]
	NS/NS	Mt/m-CN	35 W Xenon lamp	H <sub>2</sub> O/H <sub>2</sub>	CO CH <sub>4</sub>	505 330	[70]
	NS/NS	SnS <sub>2</sub> /TiO <sub>2</sub>	300 W Xe lamp	H <sub>2</sub> O	CH <sub>4</sub>	23	[71]
	NS/NS	g-C <sub>3</sub> N <sub>4</sub> /BiVO <sub>4</sub>	300 W Xe lamp $\lambda \geq 420$ nm	H <sub>2</sub> O	CO CH <sub>4</sub>	5.19 4.57	[72]
	NS/NS	PGCN/Bi <sub>12</sub> O <sub>17</sub> Cl <sub>2</sub>	300 W xenon lamp	H <sub>2</sub> O	CH <sub>4</sub>	24.4	[73]
	NP-NS/NS	Pd-g-C <sub>3</sub> N <sub>4</sub> /RGOA	300 W Xe lamp	H <sub>2</sub> O	CH <sub>4</sub>	6.4	[74]

### 3.1.1. Zero-Dimensional Structure-Based Photocatalysts for CO<sub>2</sub> Conversion

Zero-dimensional (0D) structures, namely quantum dots (QDs), are nanostructures in which the motion of electrons is spatially confined in three dimensions because of their ultrasmall size (typically, 1.2–10 nm), showing unique optical and electrical properties. With these beneficial properties, various QD photocatalysts have been demonstrated with various materials, including CdS [75], PbS [76], ZnSe [77], CuInS<sub>2</sub> [78], BiVO<sub>4</sub> [79], NiS<sub>2</sub> [80], carbon, graphene [11,81], black phosphorus [13,82], Bi<sub>2</sub>S<sub>3</sub> [83], and perovskite [45,46,48]. Other than these QD materials mentioned here, several 0D materials have been suggested as promising candidate for efficient CO<sub>2</sub> conversion.

One of those promising QD materials is carbon QDs (CQD). CQDs are small amorphous carbon nanoparticles with sp<sup>3</sup> hybridization and possess less than 10 nm in size [84]. Unlike conventional semiconductor QDs, CQDs absorb broad range of the solar spectrum extending to near infrared region due to  $\pi$ -plasmon absorption in the core carbon nanocrystals [85]. The light absorption in the UV-visible region could be ascribed to the  $\pi \rightarrow \pi^*$  transition of conjugated carbon atoms. Besides, the photoluminescent characteristics can be controlled by variation of the size of nanoparticles [86]. The excellent electronic conductivity of carbon dots causes promoted charge carrier separation and transfer. In addition, CQDs have ability to decrease the activation energy of the CO<sub>2</sub> reaction, consequently the adsorption of CO<sub>2</sub> molecules on the photocatalyst surface has been enhanced [87].

Another great candidate is graphene QDs (GQDs). GQDs are crystalline material with sp<sup>2</sup> hybridized carbon. The size of GQD is ranged between 2 and 10 nm. In the past few years, GQDs have attracted tremendous attention for energy conversion ascribed not only to the quantum confinement and edge effects but also to its electronic and physiochemical properties. GQD is noted for its oxygenated functional groups on the surface which can act as active sites for some molecules such as CO<sub>2</sub> [88].

Perovskite QDs (PQDs) are also attractive materials for 0D structure-based photocatalysts owing to their innate properties such as long diffusion length and high absorption coefficient [89,90] and their photophysical properties such as tunable band gap and high carriers mobility when they are fabricated as nanocrystals. Zhou and coworkers synthesized stable lead-free Cs<sub>2</sub>AgBiBr<sub>6</sub> perovskite QDs via hot injection method as shown in Figure 5a [47]. The synthesized QDs demonstrate the uniform distribution of cubic Cs<sub>2</sub>AgBiBr<sub>6</sub> nanocrystals with 9.5 nm of the average size when

prepared at the optimum injection temperature of 200 °C. The Cs<sub>2</sub>AgBiBr<sub>6</sub> nanocrystals (NCs) were utilized to convert CO<sub>2</sub> into solar fuels. The prepared Cs<sub>2</sub>AgBiBr<sub>6</sub> NCs possess a matched conduction band with the redox potentials of CO<sub>2</sub> to produce CH<sub>4</sub> and CO. As shown in Figure 5b, the enlarged band gap of the NCs (2.52 eV) compared to their bulk counterpart (1.95 eV) is attributed to the quantum confinement effect. The nanocrystals of Cs<sub>2</sub>AgBiBr<sub>6</sub> showed improved photocatalytic performance to reduce CO<sub>2</sub> into solar fuels compared to bulk Cs<sub>2</sub>AgBiBr<sub>6</sub>, which was 2.22 and 0.14 μmol·g<sup>-1</sup> of CO and CH<sub>4</sub>, respectively, after 6 h illumination. Zhou washed the prepared photocatalyst with ethanol to avoid the poor conductivity of the ligand layer. As plotted in Figure 5c, the washed nanocrystals boosted the evolution yield of CO<sub>2</sub> and CH<sub>4</sub> to 14.1 and 9.6 μmol·g<sup>-1</sup> after 6 h illumination. The nanostructured Cs<sub>2</sub>AgBiBr<sub>6</sub> are favorable for outstanding CO<sub>2</sub> conversion due to its efficient charge carrier transfer compared to bulk Cs<sub>2</sub>AgBiBr<sub>6</sub> [47].

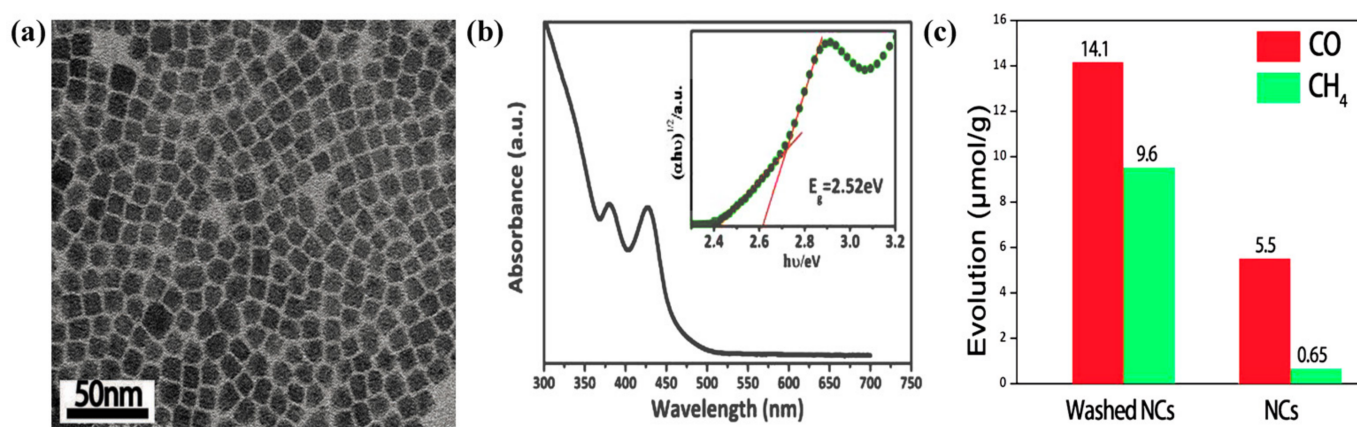


**Figure 5.** (a) TEM images of Cs<sub>2</sub>AgBiBr<sub>6</sub> NCs synthesized at different temperature at 200 °C (b) UV-Visible spectra of colloidal Cs<sub>2</sub>AgBiBr<sub>6</sub> NCs, and the inset shows the Tauc plots of colloidal Cs<sub>2</sub>AgBiBr<sub>6</sub> NCs. (c) The photocatalytic CO<sub>2</sub> reduction performance of the as-prepared Cs<sub>2</sub>AgBiBr<sub>6</sub> NCs and washed NCs (Adapted from [47]).

Black phosphorus quantum dots (BPQDs) have been regarded as rising stars in the design of photocatalysts for CO<sub>2</sub> conversion into value-added fuels. Fan and coworkers have decorated WO<sub>3</sub> nanowires by BPQD of 3–4 nm size via a hydrothermal method. The designed BPQDs/WO<sub>3</sub> photocatalyst showed a significant enhancement of CO<sub>2</sub> conversion into CO and C<sub>2</sub>H<sub>4</sub> [13]. Zhang et al. also reported that the loading of BPQDs on g-C<sub>3</sub>N<sub>4</sub> can enhance the charge carrier separation, and consequently the conversion of CO<sub>2</sub> into CO can be improved [82].

Bi<sub>2</sub>S<sub>3</sub> QDs have been suggested to be excellent candidates to improve the photocatalyst performance [83]. Guo and his coworkers have introduced Bi<sub>2</sub>S<sub>3</sub> QDs into 2D g-C<sub>3</sub>N<sub>4</sub> via a hydrothermal method. Bi<sub>2</sub>S<sub>3</sub> QDs could promote the visible light absorption, specific surface area, and the separation of photogenerated charge carriers. Consequently, the obtained nanocomposite showed higher CO<sub>2</sub> conversion into CO with production yield of 54.74 μmol·g<sup>-1</sup>.

### 3.1.2. One-Dimensional Structure-Based Photocatalyst for CO<sub>2</sub> Conversion

One-dimensional (1D) structure refers to materials where the motion of the electron is confined in two dimensions. Typically, nanowires, nanotubes, and nanorods are common morphologies for 1D nanomaterials. Owing to this unique design, the 1D structure endows materials with excellent charge transport and extended carrier lifetimes due to the unique distribution of state density coupled with intrinsically enlarged reactivity due to a large surface area in comparison with bulk materials [21,51,91,92]. To utilize these interesting features, various semiconductor materials have been fabricated with a 1D structure and these nanostructures have attracted huge attention for improving the photocatalytic con-

version of CO<sub>2</sub> into solar fuels [93]. Among the materials, we focus on several promising and interesting materials for 1D structure-based photocatalysts.

TiO<sub>2</sub> is one of the most researched photocatalytic materials due to its low cost, non-toxicity, and chemical stability. For simplicity, we say TiO<sub>2</sub> but, in reality this name describes a number of different structures and stoichiometries. Compared to TiO<sub>2</sub> nanoparticles, when they fabricated in a 1D structure, 1D-structured TiO<sub>2</sub> provides higher photoreduction performance of CO<sub>2</sub> toward solar fuels as a result of its distinct structure and properties. For instance, 1D-structured TiO<sub>2</sub> such as nanorods and nanotubes possess low recombination rates of the photogenerated charge carriers [21]. Zou et al. synthesized one dimensional TiO<sub>2</sub> nanotubes (TNT) and nanorods (TNR) by a one-step hydrothermal method [21]. TNTs have uniform open-ended tubular morphology with outer and inner diameters of 8.24 nm and 1.75 nm, respectively, as seen in Figure 6a, while TNRs were grown in the lengths of 200 nm–2 μm and diameter of 20–90 nm (Figure 6b). As shown in Figure 6c, the conversion performance of CO<sub>2</sub> over TNTs and TNRs were about 2.33-fold and 1.48-fold higher than that of TiO<sub>2</sub> nanoparticles with an average particle size of 16 nm. The enhanced performance of CO<sub>2</sub> conversion by TNT and TNR resulted in an improved charge carrier migration. It is also found that the increase in the specific surface area provides more active sites over the TiO<sub>2</sub> nanotubes [21].

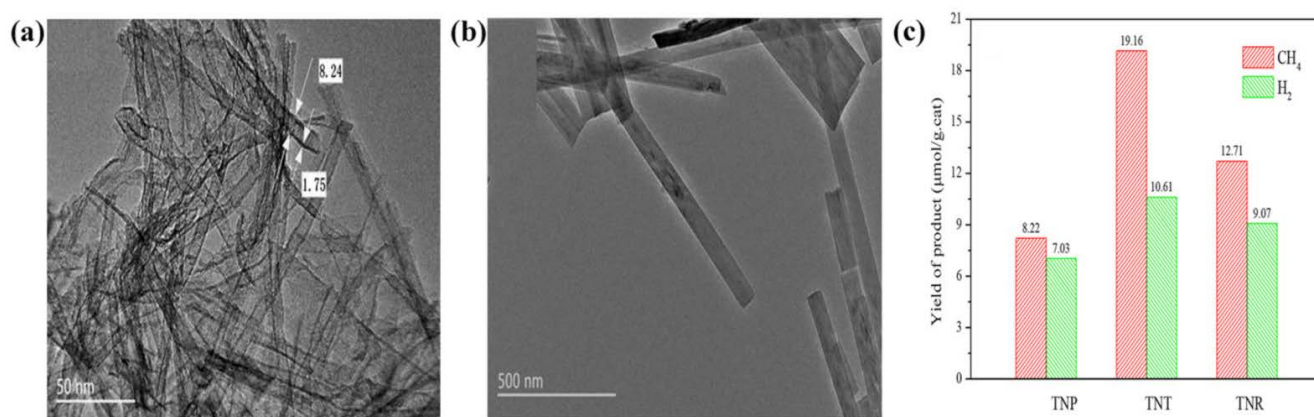


**Figure 6.** TEM images of (a) TNT and (b) TNR (c) the yield of H<sub>2</sub> and CH<sub>4</sub> after 9 h irradiation over all catalysts (Adapted from [21]).

However, TiO<sub>2</sub> is a n-type semiconductor with a band gap ranging between 3 and 3.2 eV, causing light absorption of less than 7% from AM1.5G solar spectrum and low photocatalytic activity [94–98]. To overcome these innate disadvantages of TiO<sub>2</sub>, several strategies have been demonstrated. Shankar et al. prepared TiO<sub>2</sub> nanotubes using a flame annealing method to achieve the higher CH<sub>4</sub> production yield among all TiO<sub>2</sub> stand-alone photocatalysts [99]. Liu et al. fabricated phosphate-modified TiO<sub>2</sub> nanotubes with an inner diameter of 120 nm via an impregnation method for CO<sub>2</sub> conversion into solar fuels [100]. The fabricated tubular TiO<sub>2</sub> was formed in a composite with graphitic carbon nitride (g-C<sub>3</sub>N<sub>4</sub>) through P–O bonds for photoreduction of CO<sub>2</sub> into acetic acid, formic acid, and methanol. Roy et al. fabricated multi-leg TiO<sub>2</sub> nanotubes of an average diameter of 365 nm via an electrochemical anodization method [101]. Graphene oxide was wrapped around the multi-leg nanotubes by the electrostatic interaction for further performance enhancement. Li et al. prepared reduced TiO<sub>2</sub> nanorods using a two-step hydrothermal method followed by reduction with sodium borohydride [102]. The prepared reduced TiO<sub>2</sub> nanorods exhibited higher CO<sub>2</sub> adsorption capacity due to the presence of oxygen vacancies. Holmium- and nitrogen-doped TiO<sub>2</sub> nanorods were prepared using a hydrothermal method by Hangzhou and his coworkers. The as-prepared samples exhibited higher absorption ability in the visible region [103]. Ohno et al. reported the crystal facet effect of brookite TiO<sub>2</sub> nanorods for efficient conversion of CO<sub>2</sub> into methanol [24,104]. The engineering of the facets was

achieved by a hydrothermal method using polyvinyl alcohol or polyvinyl pyrrolidone. It was found that the TiO<sub>2</sub> nanorods with mainly {210} crystal facets can act as reduction sites for CO<sub>2</sub> molecules. Amin et al. prepared TiO<sub>2</sub> nanowires with different lengths by controlling the contact time with NaOH during the reaction [105]. Gold nanoparticles were loaded on the fabricated nanowires to convert CO<sub>2</sub> into CO with evolution rate of 1237  $\mu\text{mol}\cdot\text{g}^{-1}\cdot\text{h}^{-1}$  as a result of the surface plasmonic effect of gold nanoparticles [105].

Graphitic carbon nitride (g-C<sub>3</sub>N<sub>4</sub>) is another promising material for photocatalytic CO<sub>2</sub> conversion. g-C<sub>3</sub>N<sub>4</sub> is a metal-free polymeric semiconductor photocatalyst. g-C<sub>3</sub>N<sub>4</sub> has received great attention in photocatalysis research due to its promising photocatalytic performance. A tremendous effort has been devoted to improving the photocatalytic activity of g-C<sub>3</sub>N<sub>4</sub> including elemental doping, nanostructuralization, hybridization, and surface modification [106,107]. Bulk g-C<sub>3</sub>N<sub>4</sub> exhibited inferior photocatalytic CO<sub>2</sub> reduction performance due to the low surface area and the higher recombination rate. Dimensionality control of g-C<sub>3</sub>N<sub>4</sub> has been a promising tactic to improve the CO<sub>2</sub> conversion performance to generate solar fuels. In particular, 1D-structured g-C<sub>3</sub>N<sub>4</sub> are favorable in obtaining large surface area and excellent electron-hole pair separation. Xu and coworkers have demonstrated tubular g-C<sub>3</sub>N<sub>4</sub> and explained the high reduction activity of nanotubes g-C<sub>3</sub>N<sub>4</sub> by three factors [51]: (1) the efficient charge separation because of the characteristic tubular structure (2) the higher surface area of nanotubes g-C<sub>3</sub>N<sub>4</sub> causing sufficient reactive sites and efficient CO<sub>2</sub> adsorption and (3) the promoted optical absorption. Chen and coworkers focused on the transformation of two dimensional g-C<sub>3</sub>N<sub>4</sub> nanosheets into one dimensional g-C<sub>3</sub>N<sub>4</sub> nanotubes using incorporation of phosphine gas in the reaction to produce phosphorus-doped g-C<sub>3</sub>N<sub>4</sub> nanotubes (P-g-C<sub>3</sub>N<sub>4</sub>) [50]. The morphological structure of g-C<sub>3</sub>N<sub>4</sub> nanotubes was confirmed by TEM as shown in Figure 7a. It is found that the tubes have a diameter of 200 nm and a wall thickness of 30–50 nm. As shown in Figure 7b, the as-prepared P-g-C<sub>3</sub>N<sub>4</sub> nanotubes exhibited enhancement in solar-to-fuels efficiency in comparison with that of 2D g-C<sub>3</sub>N<sub>4</sub>. The higher CO<sub>2</sub> reduction to CH<sub>4</sub> and CO ascribed not only to the enlarged surface area and extended photon absorption, but also to the band structure tailoring. Moreover, the fabricated g-C<sub>3</sub>N<sub>4</sub> nanotubes exhibited improved charge transfer, photocurrent and reduced charge transfer resistance from PL, TPC, and EIS measurements, respectively.

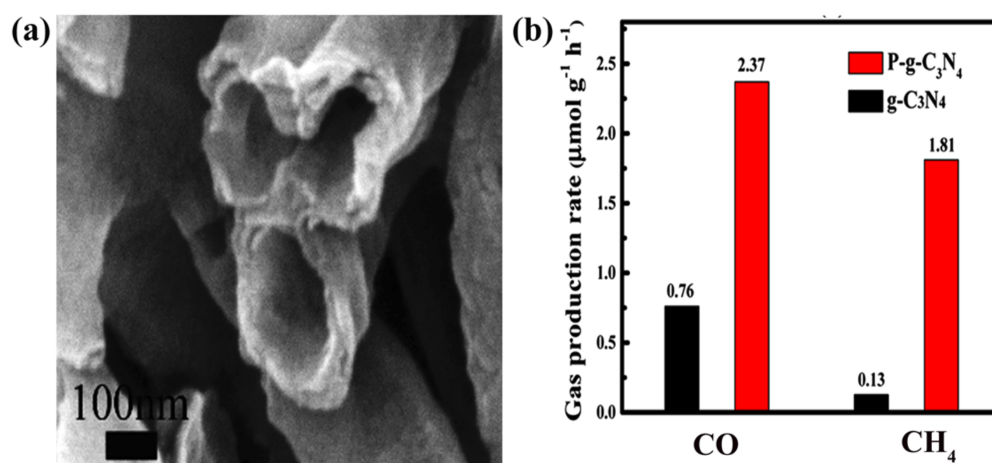


**Figure 7.** (a) TEM image of P-g-C<sub>3</sub>N<sub>4</sub> nanotubes (b) photocatalytic reduction activity for CO<sub>2</sub> conversion to produce CO and CH<sub>4</sub> of g-C<sub>3</sub>N<sub>4</sub> and P-g-C<sub>3</sub>N<sub>4</sub>, (Adapted from [50]).

### 3.1.3. Two-Dimensional Structure-Based Photocatalysts for CO<sub>2</sub> Conversion

Two-dimensional (2D) materials with thicknesses of a few atoms to <100 nm, and flake-shaped morphology are known as nanosheets (NS) [108]. Owing to the quantum confinement effect, 2D materials are characterized by distinct electronic and optical properties compared to bulk materials. However, the optical and electronic characteristics of

nanosheets are improved further when these materials are thinned to ultrathin nanosheets (mono layers) [33]. Graphene is the most common 2D material which has been studied in many fields, including photocatalysis, due to its high charge carrier mobility [109]. MoS<sub>2</sub> [110–112], WS<sub>2</sub> [113], boron nitride [114], g-C<sub>3</sub>N<sub>4</sub> [115], black phosphorus [116–118], bismuth-based materials [14,57,64,119–121], perovskite [122], and Mxene [123] have been used as 2D photocatalysts to produce solar fuels. Two dimensional materials have sparked interest for the transformation of CO<sub>2</sub> into solar fuels because the traditional semiconductor materials possess low photoreduction performance. On the other hand, 2D materials exhibited maximum surface area, minimum migration distance of photogenerated charge carriers, ability for formation of vacancy-type active sites, and dangling bonds at edges [33]. Ultrathin nanosheets forming grain boundaries-free cause facile charge carrier transfer and suppress recombination rates [124,125]. Current efforts are being focused on the development and utilization of 2D semiconductor materials to reduce CO<sub>2</sub> effectively. Here, we highlight the state-of-the-art progress in utilization of 2D photocatalysts for CO<sub>2</sub> conversion into fuels.

As reported by Ye et. al., 2D g-C<sub>3</sub>N<sub>4</sub> nanosheets can be obtained from the exfoliation of bulk g-C<sub>3</sub>N<sub>4</sub>, the g-C<sub>3</sub>N<sub>4</sub> nanosheets disperse uniformly with diameters ranging from 60 to 110 nm and a thickness of 1 nm [54]. The as-prepared 2D g-C<sub>3</sub>N<sub>4</sub> exhibited efficient solar-to-fuel conversion, CO and CH<sub>4</sub> evolution rate of 5.407  $\mu\text{mol}\cdot\text{g}^{-1}\cdot\text{h}^{-1}$  and 1.549  $\mu\text{mol}\cdot\text{g}^{-1}\cdot\text{h}^{-1}$ , respectively, which are much higher than the values of bulk-C<sub>3</sub>N<sub>4</sub> due to the higher CO<sub>2</sub> adsorption capacity of g-C<sub>3</sub>N<sub>4</sub> nanosheet compared to its bulk counterpart.

An ultrathin g-C<sub>3</sub>N<sub>4</sub> nanosheet was prepared by exfoliation of bulk g-C<sub>3</sub>N<sub>4</sub> in NH<sub>3</sub> atmosphere as reported by Jaroniec et al. [55]. An FESEM image demonstrated the ultrathin morphology of the exfoliated g-C<sub>3</sub>N<sub>4</sub> as shown in Figure 8b. Compared to the aggregated particles of bulk g-C<sub>3</sub>N<sub>4</sub> in Figure 8a, NH<sub>3</sub>-exfoliated g-C<sub>3</sub>N<sub>4</sub> is characterized with hierarchical structure assembled by ultrathin nanosheets. As shown in Figure 8c, the nanosheets consists of 9–10 layers of g-C<sub>3</sub>N<sub>4</sub> that correspond to about 3 nm of thickness. The as-prepared g-C<sub>3</sub>N<sub>4</sub> nanosheets show a higher CO<sub>2</sub> adsorption affinity (by a factor of 4) over bulk g-C<sub>3</sub>N<sub>4</sub> due to their high surface area. The quantum confinement effect shifted the band gap of 2D g-C<sub>3</sub>N<sub>4</sub> to 2.98 eV. The remarkable improvement of CO<sub>2</sub> reduction into CH<sub>4</sub> and methanol over 2D g-C<sub>3</sub>N<sub>4</sub> photocatalyst is supported by the enhanced charge separation and transfer supports as measured in TPC, EIS, and TRPL measurements (Figure 8d to Figure 8f, respectively).

Ultrathin silicon carbide (SiC) nanosheets were prepared using 2D reduced graphene oxide for artificial synthesis of CH<sub>4</sub> by Han et al. [56]. It is found that the dangling bonds from the surface of SiC NSs facilitate more effective adsorption of CO<sub>2</sub> molecules. This improves the photocatalytic performance of CO<sub>2</sub> reduction and the measured production rate of CH<sub>4</sub> by ultrathin SiC was higher than that both by bulk SiC and TiO<sub>2</sub> [56].

Intrinsic defects on the surface of photocatalysts such as oxygen vacancies [126,127], zinc vacancies [128], nitrogen vacancies [129] and bismuth vacancies [130] have a direct influence on the charge separation and transfer processes. Consequently, the photocatalytic performance of CO<sub>2</sub> reduction can be boosted. For instance, Liu and coworkers have been designed an aurivillius phase oxide, defective Bi<sub>2</sub>MoO<sub>6</sub> ultrathin NSs to improve the photocatalytic reduction of CO<sub>2</sub>. The surface defects were formed by controlling the thickness of NSs to the atomic scale to facilitate the escape of surface atoms. The as prepared NSs exhibited 2.55 times higher CO production rate than that of bulk counterpart [57].

2D nanostructured bismuth-based materials such as bismuth oxyhalide (BiOX, X = Cl, Br and I) [120], Bi<sub>2</sub>MoO<sub>6</sub> [57], Bi<sub>2</sub>WO<sub>6</sub> [64], and BiVO<sub>4</sub> [119] have been reported as promising materials for the photoconversion of CO<sub>2</sub> into solar fuels. In spite of the low-efficiency of CO<sub>2</sub> conversion over bismuth oxyhalide, there is a great interest in the development of BiOX-based photocatalysts. For instance, Zhou and coworkers have prepared oxygen vacancy BiOCl nanosheets of 4 nm thickness via a solvothermal method. The as-synthesized photocatalyst exhibits higher CO production under UV-vis irradiation compared to BiOCl. The superior CO<sub>2</sub> photoconversion over BiOCl with oxygen vacancies is attributed to the

improved exciton dissociation and enhanced photon absorption [120]. Ye et al. reported use of an ultrathin BiOBr nanosheet as a photocatalyst to improve the CO<sub>2</sub> conversion into solar fuels [121].

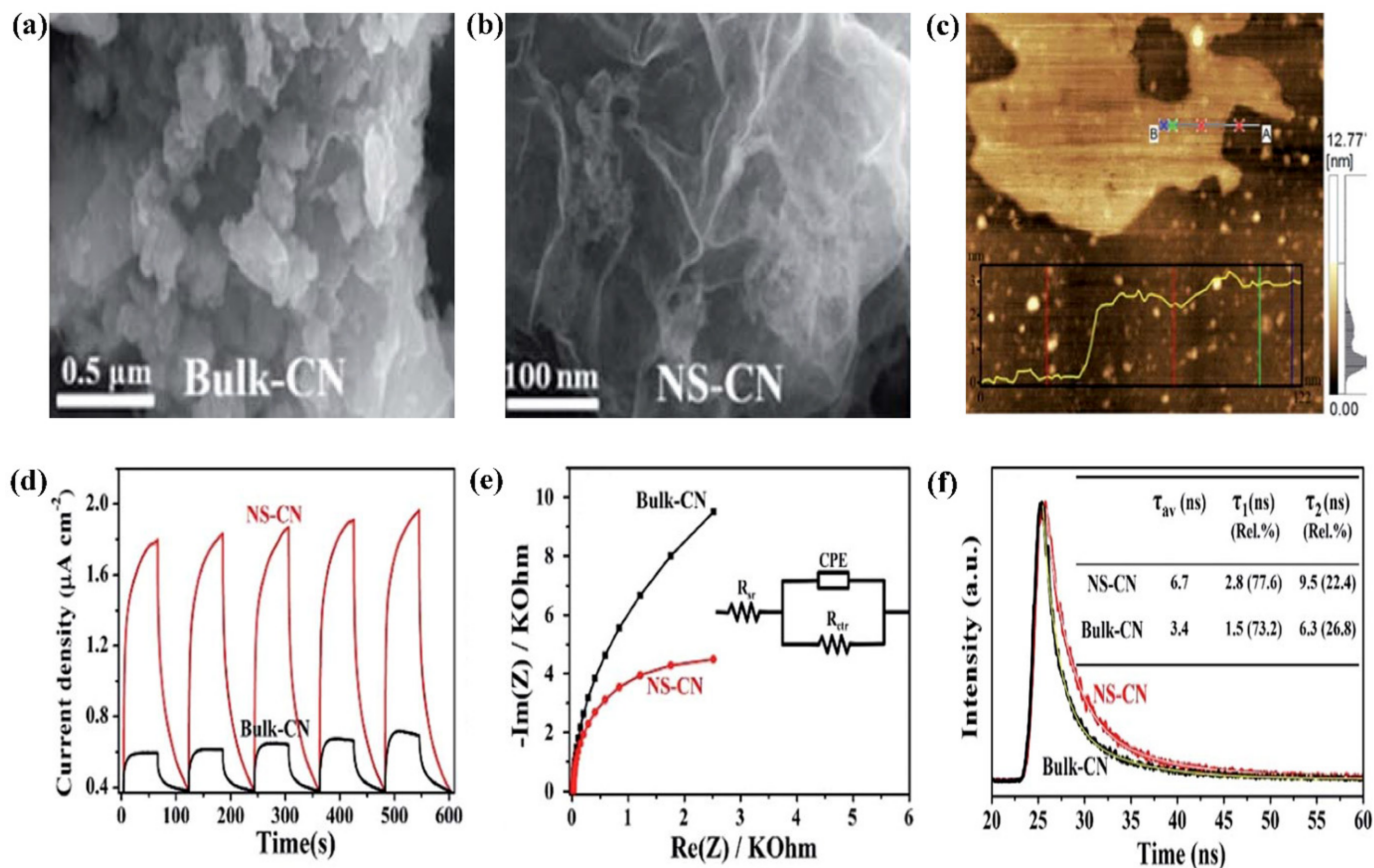


**Figure 8.** Surface morphologies of (a) bulk g-C<sub>3</sub>N<sub>4</sub> and (b) g-C<sub>3</sub>N<sub>4</sub> nanosheets, (c) atomic force microscopic image of g-C<sub>3</sub>N<sub>4</sub> nanosheets, (d) transient photocurrent responses ( $\lambda = 420$  nm), (e) electrochemical impedance spectra, and (f) time-resolved PL spectra of the bulk g-C<sub>3</sub>N<sub>4</sub> (bulk-CN) and ultrathin g-C<sub>3</sub>N<sub>4</sub> nanosheets (NS-CN) (Adapted from [55]).

The effect of halogen type in bismuth oxyhalide have been reported by Wang and his coworkers [14]. BiOX nanosheets were fabricated by hydrothermal and chemical precipitation methods. It is found that the BiOBr exhibited higher CO<sub>2</sub> conversion performance under sunlight. The formation rates of CO and CH<sub>4</sub> were 21.6 and 1.2  $\mu\text{mol}\cdot\text{g}^{-1}\cdot\text{h}^{-1}$ , respectively. It is demonstrated that the oxygen vacancies on the surface, the modest band structure, and the ionic radius of Br were responsible for the efficient production of solar fuels.

Xu et al. have prepared highly stable black phosphorus monolayers via a green exfoliation method assisted by liquid nitrogen. The photocatalyst exhibited superior CO evolution rate of 112.6  $\mu\text{mol}\cdot\text{g}^{-1}\cdot\text{h}^{-1}$  under visible light radiation. The high stability of the as-prepared photocatalyst can be attributed to the introduction of hydroxy groups during the exfoliation process. The higher performance of the black phosphorus can be ascribed to band gap engineering and enhanced charge carriers dynamics [118].

Owing to the low specific area of Dion–Jacobson perovskites, Do and coworkers fabricated a 2D-reduced perovskite, HCa<sub>2</sub>Ta<sub>3</sub>O<sub>10</sub>, decorated with Cu and Pt to improve the surface of the photocatalyst. The as-prepared photocatalyst can convert CO<sub>2</sub> into methanol and ethanol with formation rates of 7.4 and 113.2  $\mu\text{mol}\cdot\text{g}^{-1}\cdot\text{h}^{-1}$ . The photoconversion performance of CO<sub>2</sub> over the reduced perovskite was much higher than that of nonreduced perovskite due to the enhanced light absorption and the improved charge separation [122].

### 3.2. Low-Dimensional Metal Materials for CO<sub>2</sub> Conversion

Metal materials also can have unique properties when they are prepared in a low-dimensional structure. Other than the fact that improved surface area results from a morphological change on the nanoscale, low-dimensionally structured metals can show resonance of surface electrons with the presence of incident light, which is the so-called plasmonic effect. Specifically, the oscillating electric field of the incident light makes surface plasmon resonance with oscillating surface electrons on metals and the resonance help electrons to become more energetic [131]. The resonance frequency varies depending on the materials and the wavelength of the plasmon resonances in nanocrystals depends on the shape and size of nanomaterials [95,132,133]. In general, the plasmon resonance wavelength can be blue shifted with a decrease in the material size [134,135].

Nanostructured metals, in particular those fabricated with noble metals such as Ag, Au, Cu, or Pt, are of special interest because they have shown superior catalytic activity and excellent selectivity in photocatalytic applications [136,137]. The incorporation of these plasmonic metal nanomaterials can act as efficient electron sinks in the photocatalytic reactions. The semiconductor photocatalysts forming a junction with these plasmonic metal nanoparticles exhibit remarkable improvements in the charge transfer, charge separation, and recombination rate and thereby they showed highly improved photocatalytic activity [138]. In addition, the plasmonic resonance of Ag, Au, and Cu occur with visible light [139] and excitation of plasmons on the surface of conducting materials under light illumination at their plasmon wavelength have led to enhancement in photon absorption and photocurrent response [134,135].

These striking features of low-dimensional metal materials have been applied to photocatalysts and have contributed to the general enhancement of photocatalytic performance. For instance, gold NPs influence the photocatalytic reduction of CO<sub>2</sub> over TiO<sub>2</sub> due to the hot electron injection and near field enhancement that can produce more efficient electron-hole pairs at the surface of the photocatalyst. The smaller size of Au nanoparticles was significantly enhanced the charge separation over Au-modified TiO<sub>2</sub> while the larger size has direct outcome of the increased field enhancement [140]. The effect of surface plasmon resonance on TiO<sub>2</sub> nanotubes was studied by Cheng and coworkers, Silver (Ag) nanoparticles were loaded on TiO<sub>2</sub> nanotubes via an electrochemical deposition method to inject hot electrons to the nanotubes and accelerate the migration of electron-hole pairs to the photocatalyst surface [141]. The Ag nanoparticles have been shown to enhance the utilization of visible light. Consequently, the photocatalytic conversion of CO<sub>2</sub> into CH<sub>4</sub> and other hydrocarbon species is improved compared to the as-prepared nanotubes without Ag deposition and TiO<sub>2</sub> nanoparticles.

## 4. Strategies for Enhancement in the Light-Driven CO<sub>2</sub> Conversion over Low-Dimensional Photocatalysts

Applying low-dimensional structure to the photocatalytic system itself is a proven way for obtaining high CO<sub>2</sub> conversion performance. However, further improvement is available by designing the structures or modifying the photocatalytic materials so that characteristics of photocatalysts or photocatalytic system are engineered. Here, we focus on these two major strategies for further enhancement of CO<sub>2</sub> conversion by low-dimensional photocatalysts. Table 2 summarizes the examples mentioned in this section.

### 4.1. Construction of Junction Formed by Low-Dimensional Structures

Of the diverse strategies to promote CO<sub>2</sub> conversion performance of photocatalysts, designing or formation of junctions in photocatalytic systems has seen some success by modifying optical and electrical properties through materials and interfaces [63]. Junctions are constructed by coupling of two or more semiconductor materials or metal materials. The formation of a junction allows valuable properties from various materials to be more available in a single system. That helps more efficient light absorption, charge separation and transfer, or more stable performance. Since the photocatalytic systems with junctions

have single or multiple interfaces, the engineering of the interfacial characteristics between the materials is essential for efficient photocatalyst performance. Especially, the interface characteristics can influence on carrier behaviors through bulk or at interfaces (ex. Shockley-Read-Hall recombination).

The formation of junctions implies the presence of an internal electric field in the nanomaterial. This internal electric field can contribute to enhanced carrier behaviors such as carrier separation and transfer for the photo-induced charge carriers and to, in the end, the performance of light-driven CO<sub>2</sub> conversion. The internal electric field can be induced by growth of a low-dimensional semiconductor on a low-dimensional semiconductor [23,107]. The combination of two or multiple low-dimensional materials could integrate the advantages of both single units and mitigate the shortcomings of single unit by the synergistic effect [142].

One of the advantages of semiconductor QDs is the quantum size effect which is responsible for the optical properties of the photocatalyst. Apart from the acceleration of charge separation and transfer process, the contact between 0D semiconductor and 1D semiconductor provides the nanocomposite with an additional properties such as excessive electroactive sites, high surface area, and homogenous dispersion [143]. 1D Bi<sub>2</sub>S<sub>3</sub> nanotubes have outstanding ability to absorb visible and near infrared light. The tubular structure of Bi<sub>2</sub>S<sub>3</sub> provides the photocatalytic reaction with more active sites than other morphologies [58]. The remarkable optical and electronic properties of tungsten disulfide (WS<sub>2</sub>) QDs can be realized due to the quantum confinement effect. WS<sub>2</sub> QDs can be also dispersed uniformly on the surface of Bi<sub>2</sub>S<sub>3</sub> forming Bi-S channels to facilitate the charge carrier separation transfer process. The designed 0D/1D nanocomposite exhibited outstanding photocatalytic reduction of CO<sub>2</sub> into CH<sub>3</sub>OH and C<sub>2</sub>H<sub>5</sub>OH of 38.2 μmol·g<sup>-1</sup> and 27.8 μmol·g<sup>-1</sup> after 4 h radiation, respectively. The improved photoreduction performance is related to the following features. Firstly, the 0D/1D nanocomposite provided combined optical and electrical properties of both WS<sub>2</sub> QDs and Bi<sub>2</sub>S<sub>3</sub> nanotubes causing high visible and near infrared light absorption. Secondly, the enlarged surface area of the nanocomposite provided more active adsorptions site for CO<sub>2</sub>. Thirdly, the low resistive QDs-NTs interface due to the Bi-S bonds plays a critical role for accelerated charge carrier separation [58]. CsPbBr<sub>3</sub> is widely used in the photocatalytic reactions but it suffers from the high rate of recombination during the interface transfer due to the strong reductive ability of electrons [64]. Hence, the suppression of undesired electron loss throughout the transfer process at the interface is critical factor for efficient utilization of CsPbBr<sub>3</sub>. Li et al. fabricated 0D/2D nanocomposite of CsPbBr<sub>3</sub>/Bi<sub>2</sub>WO<sub>6</sub> via ultrasonic method with intimate contact at the interface to improve the charge separation and transfer. The Bi-Br bonds which is formed at the QDs-NSs interface is responsible for the strong interfacial interaction. The decoration of Bi<sub>2</sub>WO<sub>6</sub> with CsPbBr<sub>3</sub> QDs could enhance the CO and CH<sub>4</sub> yield by factor of 9.5 over that of pristine CsPbBr<sub>3</sub> [64].

The building of 1D semiconductor materials on 2D semiconductors is an efficient strategy for efficient CO<sub>2</sub> conversion. Coupling of TiO<sub>2</sub> nanofibers with light harvesting semiconductors such as MoS<sub>2</sub> nanosheets is an efficient way to overcome the fast recombination of charge carriers and enhance the light absorption efficiency [65]. The electronic properties of MoS<sub>2</sub> nanosheets can be tuned by control of the thickness. The superior conversion activity of CO<sub>2</sub> into hydrocarbon species, that is, CH<sub>4</sub> and CH<sub>3</sub>OH, resulted from the improved light harvesting, sufficient reactive sites for CO<sub>2</sub> adsorption, and the intimate 1D-2D chemical contact between MoS<sub>2</sub> and TiO<sub>2</sub> which could be favorable for facile and efficient charge separation upon photoexcitation [65]. The increase of the contact area between the two semiconductor nanomaterials is much more favorable to enhance the photocatalytic performance over the photocatalyst. In other words, constructing the 2D/2D interface is favorable for highly separated charge carriers at the interface. Wang et al. prepared 2D/2D heterojunctions by growth of ultrathin tin disulfide (SnS<sub>2</sub>) onto TiO<sub>2</sub> nanosheets via a hydrothermal method [71]. The production yield of CH<sub>4</sub> over SnS<sub>2</sub>/TiO<sub>2</sub> was much higher than that of pristine SnS<sub>2</sub> and TiO<sub>2</sub> nanosheets. The reason for such

outstanding performance originates from the increment of the contact area between SnS<sub>2</sub> and TiO<sub>2</sub> nanosheets [71].

The photocatalytic systems with multiple junctions, that is, with multiple interfaces, displays excellent photocatalytic activity toward solar fuels generation compared to one with/without single junction [67,144,145]. Recently, Macyk and coworkers designed two heterointerface-based photocatalyst, TiO<sub>2</sub>/C<sub>3</sub>N<sub>4</sub>/Ti<sub>3</sub>C<sub>2</sub>, via the interfacial assembly of Ti<sub>3</sub>C<sub>2</sub> QDs on the TiO<sub>2</sub>/C<sub>3</sub>N<sub>4</sub> binary nanocomposite to boost the charge separation and transfer and providing strong redox ability in CO<sub>2</sub> photoreduction reaction [145]. The as-synthesized composite exhibited enhanced light absorption, suppressed electron-hole recombination, and demonstrated stable photocurrent sensitivity. The fabricated composite could overcome the disadvantage of TiO<sub>2</sub>/C<sub>3</sub>N<sub>4</sub> nanocomposites with a single junction by providing more efficient transport channels of electrons-hole pairs due to the strong interaction between Ti<sub>3</sub>C<sub>2</sub> QDs and TiO<sub>2</sub>/C<sub>3</sub>N<sub>4</sub> NS. Theoretical studies demonstrated that construction of two interfacial electric fields between TiO<sub>2</sub>/C<sub>3</sub>N<sub>4</sub> and Ti<sub>3</sub>C<sub>2</sub>/C<sub>3</sub>N<sub>4</sub> is due to electron transfer processes at the two interfaces. The interfacial built-in electric fields can promote the charge carrier separation and the photocatalytic reduction of CO<sub>2</sub> into CO and CH<sub>4</sub>. Tonda et al. fabricated another multijunction system with a Bi<sub>2</sub>WO<sub>3</sub>/RGO/g-C<sub>3</sub>N<sub>4</sub> 2D/2D/2D architecture using two-step hydrothermal method for utilization in CO<sub>2</sub> and water reduction into useful fuels [144]. This ternary heterojunction exhibited highly improved characteristics in light harvesting ability, CO<sub>2</sub> adsorption capacity, photocurrent responses, and interfacial contact area. The photoconversion performance of CO<sub>2</sub> over Bi<sub>2</sub>WO<sub>3</sub>/RGO/g-C<sub>3</sub>N<sub>4</sub> was dramatically enhanced toward CH<sub>4</sub> and CO evolution. The performance of Bi<sub>2</sub>WO<sub>3</sub>/RGO/g-C<sub>3</sub>N<sub>4</sub> was 2.5 times higher and 3.8 times higher than those of Bi<sub>2</sub>WO<sub>3</sub>/RGO and RGO/g-C<sub>3</sub>N<sub>4</sub>, respectively [144].

#### 4.2. Modification of Low-Dimensional Nanomaterials

Modification of nanostructured low-dimensional photocatalysts themselves are another beneficial strategy for the enhancement of photocatalytic CO<sub>2</sub> conversion because it helps the properties of photocatalysts to be engineered. The modification can be achieved using several approaches such as introduction of surface oxygen vacancies or the formation of a porous structure.

The efficient utilization of the solar spectrum can be controlled by tuning the band structure of the semiconductor using the elemental doping [19]. Yu et al. synthesized oxygen-doped g-C<sub>3</sub>N<sub>4</sub> nanotubes via exfoliation and a 3D g-C<sub>3</sub>N<sub>4</sub> curling condensation method [146]. It was found that the synthesized photocatalyst consisted of curled nanosheets that had a uniform tubular structure with 20–30 nm of diameter. The oxygen atoms can substitute for the C or N atoms in g-C<sub>3</sub>N<sub>4</sub> under high temperature oxidation conditions. The oxygen doping of 1D g-C<sub>3</sub>N<sub>4</sub> helped the conduction band to be at a more positive potential causing a narrower band gap and efficient light harvesting. This structure exhibited a significant methanol evolution rate of 0.88 μmol·g<sup>-1</sup>·h<sup>-1</sup> under visible light radiation. Wu et al. synthesized self-doped black TiO<sub>2</sub> nanotubes arrays using a one-step aluminothermic reduction for solar-driven conversion of CO<sub>2</sub> into CO [147]. It is found that the average diameter of the nanotubes was 75–85 nm with 5–7 nm of wall thickness. The oxygen vacancies can act as active sites for CO<sub>2</sub> molecules for efficient photogenerated charge carrier separation. The visible light absorption of black TiO<sub>2</sub> was largely enhanced by virtue of the oxygen vacancies. The resulted photocatalytic conversion was 185.39 μmol·g<sup>-1</sup>·h<sup>-1</sup> of CO evolution rate under visible light.

The introduction of defects into semiconductors can improve the photocatalytic activity of CO<sub>2</sub> into solar fuels ascribed to the promotion of photogenerated charge carrier separation and the extended light absorption [148]. Liu and coworkers prepared Bi<sub>12</sub>O<sub>17</sub>Cl<sub>2</sub> nanotubes with surface oxygen defects via solvothermal method [52]. The tubular structure plays crucial role for accelerating the photogenerated charge carrier separation, while the oxygen defects on the surface act as active centers for CO<sub>2</sub> activation. It is found that the absorption of Bi<sub>12</sub>O<sub>17</sub>Cl<sub>2</sub> nanotubes is improved in the visible region compared to its bulk counterpart. The defective ultrathin tubular structure of Bi<sub>12</sub>O<sub>17</sub>Cl<sub>2</sub> provides effective CO<sub>2</sub>

conversion into CO with production yield of 16.8 times higher than bulk  $\text{Bi}_{12}\text{O}_{17}\text{Cl}_2$ . The higher photocatalytic conversion rate can be attributed to faster charge separation on the surface of  $\text{Bi}_{12}\text{O}_{17}\text{Cl}_2$  nanotubes.

The porosity of nanostructured semiconductors provides an additional feature to increase the surface area of photocatalysts, and subsequently is favorable for the solar-driven reduction of  $\text{CO}_2$  into valuable fuels [149]. Huang et al. used a template-free method to prepare porous g- $\text{C}_3\text{N}_4$  with increased surface area [150]. It is reported that the porous g- $\text{C}_3\text{N}_4$  nanotubes had excellent photocatalytic conversion of  $\text{CO}_2$  into CO of  $40 \mu\text{mol}\cdot\text{g}^{-1}$  within 4 h illumination. The CO yield was higher than that of bulk g- $\text{C}_3\text{N}_4$  by a factor of 5.6 originated from the higher surface area of the porous tubular structure, and the improved charge carrier separation and transfer process.

## 5. Conclusions

The solar-driven conversion of  $\text{CO}_2$  into valuable fuels such as methane, carbon dioxide, methanol, ethanol, acetaldehyde, and formaldehyde, can be an effective way to simultaneously mitigate the effects of global warming and solve energy crisis all over the world. In this work, following a brief introduction of the essential need to decrease the greenhouse gas effect caused by the excessive emission of  $\text{CO}_2$ , the photocatalytic reduction process of  $\text{CO}_2$  was discussed including the three basic steps: first, light absorption via the photocatalyst to generate electron-hole pairs; second, separation of the photogenerated charge carriers and transfer to the photocatalyst surface; and third, reaction of the photogenerated electrons and holes with  $\text{CO}_2$  and water, respectively, to produce solar fuels. The high-efficiency conversion of  $\text{CO}_2$  into chemical fuels requires a balance between the following consideration of the photocatalyst: firstly, the low band gap of the semiconductor is required for enhanced light absorption provided that the CBM and VBM matching with the redox potentials of the reactants. Secondly, the conversion of  $\text{CO}_2$  into solar fuels is also dependent on the surface area of the photocatalyst which can facilitate the adsorption of the  $\text{CO}_2$  molecules on the semiconductor surface. Thirdly, the charge dynamics process, namely, e-h separation/transfer, must be controlled to minimize the fast recombination of the photogenerated charge carriers. In this regard, several strategies have been reported to improve the  $\text{CO}_2$  conversion including elemental doping, heterojunction construction, surface modification, nanostructuralization, and dimensionality reduction. A review was presented of the advantages of nanostructured low-dimensional photocatalysts, including the higher surface area, the suppressed recombination rate due to its crystallinity, the quantum confinement effect in semiconductors, and plasmonic effect on the surface of metals nanoparticles. Further, the state-of-the-art progress of 0D, 1D, and 2D nanomaterials for  $\text{CO}_2$  reduction into solar fuels was presented. Finally, we report on two strategies to boost the photocatalytic activity of  $\text{CO}_2$  into valuable fuels: first, designing junction structures to enhance the photogenerated charge carrier separation and transfer to the surface and second the modification of low-dimensional photocatalysts using doping or porosity to enhance the light absorption and surface area. By tuning the dimensionality of nanostructured semiconductors, we are able to improve the optical and electronic properties, allowing significant enhancement of the  $\text{CO}_2$  conversion into solar fuels. Ultimately, for solar-driven conversion of  $\text{CO}_2$  into usable fuel to make an impact on society, efficient processes will also have to be inexpensive to fabricate and easily scalable. Engineered low-dimensional materials photocatalytic materials show great promise toward this end.

**Author Contributions:** Conceptualization, supervision, project administration, funding acquisition, H.L.; writing-original draft preparation, H.L., H.A.E.O., M.W.H.; writing-review and editing, H.L., M.W.H.; visualization, H.A.E.O. All authors have read and agreed to the published version of the manuscript.

**Funding:** This research was funded by the Ministry of Science and Technology of Taiwan, grant no. 109-2218-E-110-005-MY2.

**Data Availability Statement:** Data sharing not applicable.

**Acknowledgments:** The authors acknowledge the financial support of the Ministry of Science and Technology of Taiwan, grant no. 109-2218-E-110-005-MY2.

**Conflicts of Interest:** The authors declare no conflict of interest.

## References

1. Halmann, M. Photoelectrochemical reduction of aqueous carbon dioxide on p-type gallium phosphide in liquid junction solar cells. *Nature* **1978**, *275*, 115–116. [[CrossRef](#)]
2. Hemminger, J.; Carr, R.; Somorjai, G. The photoassisted reaction of gaseous water and carbon dioxide adsorbed on the SrTiO<sub>3</sub> (111) crystal face to form methane. *Chem. Phys. Lett.* **1978**, *57*, 100–104. [[CrossRef](#)]
3. Inoue, T.; Fujishima, A.; Konishi, S.; Honda, K. Photoelectrocatalytic reduction of carbon dioxide in aqueous suspensions of semiconductor powders. *Nature* **1979**, *277*, 637–638. [[CrossRef](#)]
4. Zeng, S.; Kar, P.; Thakur, U.K.; Shankar, K. A review on photocatalytic CO<sub>2</sub> reduction using perovskite oxide nanomaterials. *Nanotechnology* **2018**, *29*, 052001. [[CrossRef](#)]
5. Zhou, B.; Song, J.; Xie, C.; Chen, C.; Qian, Q.; Han, B. Mo–Bi–Cd Ternary Metal Chalcogenides: Highly Efficient Photocatalyst for CO<sub>2</sub> Reduction to Formic Acid Under Visible Light. *ACS Sustain. Chem. Eng.* **2018**, *6*, 5754–5759. [[CrossRef](#)]
6. Bie, C.; Zhu, B.; Xu, F.; Zhang, L.; Yu, J. In situ grown monolayer N-doped graphene on CdS hollow spheres with seamless contact for photocatalytic CO<sub>2</sub> reduction. *Adv. Mater.* **2019**, *31*, 1902868. [[CrossRef](#)] [[PubMed](#)]
7. Billo, T.; Shown, I.; Kumar Anbalagan, A.; Effendi, T.A.; Sabbah, A.; Fu, F.-Y.; Chu, C.-M.; Woon, W.-Y.; Chen, R.-S.; Lee, C.-H. A mechanistic study of molecular CO<sub>2</sub> interaction and adsorption on carbon implanted SnS<sub>2</sub> thin film for photocatalytic CO<sub>2</sub> reduction activity. *Nano Energy* **2020**, *72*, 104717. [[CrossRef](#)]
8. Li, D.; Kassymova, M.; Cai, X.; Zang, S.-Q.; Jiang, H.-L. Photocatalytic CO<sub>2</sub> reduction over metal-organic framework-based materials. *Coord. Chem. Rev.* **2020**, *412*, 213262. [[CrossRef](#)]
9. Liu, W.; Li, X.; Wang, C.; Pan, H.; Liu, W.; Wang, K.; Zeng, Q.; Wang, R.; Jiang, J. A scalable general synthetic approach toward ultrathin imine-linked two-dimensional covalent organic framework nanosheets for photocatalytic CO<sub>2</sub> reduction. *J. Am. Chem. Soc.* **2019**, *141*, 17431–17440. [[CrossRef](#)]
10. Yang, C.; Huang, W.; da Silva, L.C.; Zhang, K.A.; Wang, X. Functional conjugated polymers for CO<sub>2</sub> reduction using visible light. *Chem. Eur. J.* **2018**, *24*, 17454–17458. [[CrossRef](#)] [[PubMed](#)]
11. Yan, Y.; Chen, J.; Li, N.; Tian, J.; Li, K.; Jiang, J.; Liu, J.; Tian, Q.; Chen, P. Systematic bandgap engineering of graphene quantum dots and applications for photocatalytic water splitting and CO<sub>2</sub> reduction. *ACS Nano* **2018**, *12*, 3523–3532. [[CrossRef](#)] [[PubMed](#)]
12. Sun, Z.; Wang, H.; Wu, Z.; Wang, L. g-C<sub>3</sub>N<sub>4</sub> based composite photocatalysts for photocatalytic CO<sub>2</sub> reduction. *Catal. Today* **2018**, *300*, 160–172. [[CrossRef](#)]
13. Gao, W.; Bai, X.; Gao, Y.; Liu, J.; He, H.; Yang, Y.; Han, Q.; Wang, X.; Wu, X.; Wang, J. Anchoring of black phosphorus quantum dots onto WO<sub>3</sub> nanowires to boost photocatalytic CO<sub>2</sub> conversion into solar fuels. *Chem. Comm.* **2020**, *56*, 7777–7780. [[CrossRef](#)]
14. Ren, X.; Gao, M.; Zhang, Y.; Zhang, Z.; Cao, X.; Wang, B.; Wang, X. Photocatalytic reduction of CO<sub>2</sub> on BiOX: Effect of halogen element type and surface oxygen vacancy mediated mechanism. *Appl. Catal. B* **2020**, *274*, 119063. [[CrossRef](#)]
15. Wang, H.; Zhang, L.; Wang, K.; Sun, X.; Wang, W. Enhanced photocatalytic CO<sub>2</sub> reduction to methane over WO<sub>3</sub>·0.33 H<sub>2</sub>O via Mo doping. *Appl. Catal. B* **2019**, *243*, 771–779. [[CrossRef](#)]
16. Gao, M.; Yang, J.; Sun, T.; Zhang, Z.; Zhang, D.; Huang, H.; Lin, H.; Fang, Y.; Wang, X. Persian buttercup-like BiOBr<sub>x</sub>Cl<sub>1-x</sub> solid solution for photocatalytic overall CO<sub>2</sub> reduction to CO and O<sub>2</sub>. *Appl. Catal. B* **2019**, *243*, 734–740. [[CrossRef](#)]
17. Samanta, S.; Yadav, R.; Kumar, A.; Sinha, A.K.; Srivastava, R. Surface modified C, O co-doped polymeric g-C<sub>3</sub>N<sub>4</sub> as an efficient photocatalyst for visible light assisted CO<sub>2</sub> reduction and H<sub>2</sub>O<sub>2</sub> production. *Appl. Catal. B* **2019**, *259*, 118054. [[CrossRef](#)]
18. Shi, R.; Chen, Y. Controlled formation of defective shell on TiO<sub>2</sub> (001) facets for enhanced photocatalytic CO<sub>2</sub> reduction. *ChemCatChem* **2019**, *11*, 2270–2276. [[CrossRef](#)]
19. Tu, W.; Zhou, Y.; Zou, Z. Photocatalytic conversion of CO<sub>2</sub> into renewable hydrocarbon fuels: State-of-the-art accomplishment, challenges, and prospects. *Adv. Mater.* **2014**, *26*, 4607–4626. [[CrossRef](#)]
20. Razzaq, A.; In, S.-I. TiO<sub>2</sub> based nanostructures for photocatalytic CO<sub>2</sub> conversion to valuable chemicals. *Micromachines* **2019**, *10*, 326. [[CrossRef](#)]
21. Huang, C.-Y.; Guo, R.-T.; Pan, W.-G.; Tang, J.-Y.; Zhou, W.-G.; Liu, X.-Y.; Qin, H.; Jia, P.-Y. One-dimension TiO<sub>2</sub> nanostructures with enhanced activity for CO<sub>2</sub> photocatalytic reduction. *Appl. Surf. Sci.* **2019**, *464*, 534–543. [[CrossRef](#)]
22. Patil, S.B.; Basavarajappa, P.S.; Ganganagappa, N.; Jyothi, M.; Raghu, A.; Reddy, K.R. Recent advances in non-metals-doped TiO<sub>2</sub> nanostructured photocatalysts for visible-light driven hydrogen production, CO<sub>2</sub> reduction and air purification. *Int. J. Hydrog. Energy* **2019**, *44*, 13022–13039. [[CrossRef](#)]
23. Xu, H.-M.; Wang, H.-C.; Shen, Y.; Lin, Y.-H.; Nan, C.-W. Low-dimensional nanostructured photocatalysts. *J. Adv. Ceram.* **2015**, *4*, 159–182. [[CrossRef](#)]
24. Chang, X.; Wang, T.; Gong, J. CO<sub>2</sub> photo-reduction: Insights into CO<sub>2</sub> activation and reaction on surfaces of photocatalysts. *Energy Environ. Sci.* **2016**, *9*, 2177–2196. [[CrossRef](#)]
25. Mao, J.; Li, K.; Peng, T. Recent advances in the photocatalytic CO<sub>2</sub> reduction over semiconductors. *Catal. Sci. Technol.* **2013**, *3*, 2481–2498. [[CrossRef](#)]

26. Markovits, A.; Fahmi, A.; Minot, C. A theoretical study of CO<sub>2</sub> adsorption on TiO<sub>2</sub>. *J. Mol. Struct. THEOCHEM* **1996**, *371*, 219–235. [[CrossRef](#)]
27. Sharma, N.; Das, T.; Kumar, S.; Bhosale, R.; Kabir, M.; Ogale, S. Photocatalytic activation and reduction of CO<sub>2</sub> to CH<sub>4</sub> over single phase nano Cu<sub>3</sub>SnS<sub>4</sub>: A combined experimental and theoretical study. *ACS Appl. Energy Mater.* **2019**, *2*, 5677–5685. [[CrossRef](#)]
28. Indrakanti, V.P.; Kubicki, J.D.; Schobert, H.H. Photoinduced activation of CO<sub>2</sub> on Ti-based heterogeneous catalysts: Current state, chemical physics-based insights and outlook. *Energy Environ. Sci.* **2009**, *2*, 745–758. [[CrossRef](#)]
29. Álvarez, A.; Borges, M.; Corral-Pérez, J.J.; Olcina, J.G.; Hu, L.; Cornu, D.; Huang, R.; Stoian, D.; Urakawa, A. CO<sub>2</sub> activation over catalytic surfaces. *ChemPhysChem* **2017**, *18*, 3135–3141. [[CrossRef](#)]
30. Fu, J.; Jiang, K.; Qiu, X.; Yu, J.; Liu, M. Product selectivity of photocatalytic CO<sub>2</sub> reduction reactions. *Mater. Today* **2020**, *32*, 222–243. [[CrossRef](#)]
31. Linsebigler, A.L.; Lu, G.; Yates, J.T., Jr. Photocatalysis on TiO<sub>2</sub> surfaces: Principles, mechanisms, and selected results. *Chem. Rev.* **1995**, *95*, 735–758. [[CrossRef](#)]
32. Khan, A.A.; Tahir, M. Recent advancements in engineering approach towards design of photo-reactors for selective photocatalytic CO<sub>2</sub> reduction to renewable fuels. *J. CO<sub>2</sub> Util.* **2019**, *29*, 205–239. [[CrossRef](#)]
33. Sun, Z.; Talreja, N.; Tao, H.; Texter, J.; Muhler, M.; Strunk, J.; Chen, J. Catalysis of carbon dioxide photoreduction on nanosheets: Fundamentals and challenges. *Angew. Chem. Int. Ed.* **2018**, *57*, 7610–7627. [[CrossRef](#)] [[PubMed](#)]
34. Yoffe, A.D. Low-dimensional systems: Quantum size effects and electronic properties of semiconductor microcrystallites (zero-dimensional systems) and some quasi-two-dimensional systems. *Adv. Phys.* **1993**, *42*, 173–262. [[CrossRef](#)]
35. Lim, Y.; Lee, D.-K.; Kim, S.M.; Park, W.; Cho, S.Y.; Sim, U. Low dimensional carbon-based catalysts for efficient photocatalytic and photo/electrochemical water splitting reactions. *Materials* **2020**, *13*, 114. [[CrossRef](#)] [[PubMed](#)]
36. Ren, X.; Philo, D.; Li, Y.; Shi, L.; Chang, K.; Ye, J. Recent advances of low-dimensional phosphorus-based nanomaterials for solar-driven photocatalytic reactions. *Coord. Chem. Rev.* **2020**, *424*, 213516. [[CrossRef](#)]
37. Peng, W.; Li, Y.; Zhang, F.; Zhang, G.; Fan, X. Roles of two-dimensional transition metal dichalcogenides as cocatalysts in photocatalytic hydrogen evolution and environmental remediation. *Ind. Eng. Chem. Res.* **2017**, *56*, 4611–4626. [[CrossRef](#)]
38. Chowdhury, C.; Karmakar, S.; Datta, A. Monolayer group IV–VI monochalcogenides: Low-dimensional materials for photocatalytic water splitting. *J. Phys. Chem. C* **2017**, *121*, 7615–7624. [[CrossRef](#)]
39. Dai, C.; Liu, B. Conjugated polymers for visible-light-driven photocatalysis. *Energy Environ. Sci.* **2020**, *13*, 24–52. [[CrossRef](#)]
40. Huynh, K.A.; Nguyen, D.L.T.; Nguyen, V.H.; Vo, D.V.N.; Trinh, Q.T.; Nguyen, T.P.; Kim, S.Y.; Le, Q.V. Halide perovskite photocatalysis: Progress and perspectives. *J. Chem. Technol. Biotechnol.* **2020**, *95*, 2579–2596. [[CrossRef](#)]
41. Khan, M.S.; Zhang, F.; Osada, M.; Mao, S.S.; Shen, S. Graphitic Carbon Nitride-Based Low-Dimensional Heterostructures for Photocatalytic Applications. *Sol. RRL* **2020**, *4*, 1900435. [[CrossRef](#)]
42. Zhao, J.; Holmes, M.A.; Osterloh, F.E. Quantum confinement controls photocatalysis: A free energy analysis for photocatalytic proton reduction at CdSe nanocrystals. *ACS Nano* **2013**, *7*, 4316–4325. [[CrossRef](#)]
43. Qamar, S.; Lei, F.; Liang, L.; Gao, S.; Liu, K.; Sun, Y.; Ni, W.; Xie, Y. Ultrathin TiO<sub>2</sub> flakes optimizing solar light driven CO<sub>2</sub> reduction. *Nano Energy* **2016**, *26*, 692–698. [[CrossRef](#)]
44. Li, A.; Wang, T.; Li, C.; Huang, Z.; Luo, Z.; Gong, J. Adjusting the reduction potential of electrons by quantum confinement for selective photoreduction of CO<sub>2</sub> to methanol. *Angew. Chem. Int. Ed.* **2019**, *58*, 3804–3808. [[CrossRef](#)] [[PubMed](#)]
45. Hou, J.; Cao, S.; Wu, Y.; Gao, Z.; Liang, F.; Sun, Y.; Lin, Z.; Sun, L. Inorganic colloidal perovskite quantum dots for robust solar CO<sub>2</sub> reduction. *Chem. Eur. J.* **2017**, *23*, 9481–9485. [[CrossRef](#)] [[PubMed](#)]
46. Sheng, J.; He, Y.; Li, J.; Yuan, C.; Huang, H.; Wang, S.; Sun, Y.; Wang, Z.; Dong, F. Identification of halogen-associated active sites on bismuth-based perovskite quantum dots for efficient and selective CO<sub>2</sub>-to-CO photoreduction. *ACS Nano* **2020**, *14*, 13103–13114. [[CrossRef](#)]
47. Zhou, L.; Xu, Y.F.; Chen, B.X.; Kuang, D.B.; Su, C.Y. Synthesis and Photocatalytic Application of Stable Lead-Free Cs<sub>2</sub>AgBiBr<sub>6</sub> Perovskite Nanocrystals. *Small* **2018**, *14*, 1703762. [[CrossRef](#)] [[PubMed](#)]
48. Que, M.; Zhao, Y.; Pan, L.; Yang, Y.; He, Z.; Yuan, H.; Chen, J.; Zhu, G. Colloidal formamidinium lead bromide quantum dots for photocatalytic CO<sub>2</sub> reduction. *Mater. Lett.* **2021**, *282*, 128695. [[CrossRef](#)]
49. Zhu, C.; Wei, X.; Li, W.; Pu, Y.; Sun, J.; Tang, K.; Wan, H.; Ge, C.; Zou, W.; Dong, L. Crystal-Plane Effects of CeO<sub>2</sub> {110} and CeO<sub>2</sub> {100} on Photocatalytic CO<sub>2</sub> Reduction: Synergistic Interactions of Oxygen Defects and Hydroxyl Groups. *ACS Sustain. Chem. Eng.* **2020**, *8*, 14397–14406. [[CrossRef](#)]
50. Liu, B.; Ye, L.; Wang, R.; Yang, J.; Zhang, Y.; Guan, R.; Tian, L.; Chen, X. Phosphorus-doped graphitic carbon nitride nanotubes with amino-rich surface for efficient CO<sub>2</sub> capture, enhanced photocatalytic activity, and product selectivity. *ACS Appl. Mater. Interfaces* **2018**, *10*, 4001–4009. [[CrossRef](#)]
51. Mo, Z.; Zhu, X.; Jiang, Z.; Song, Y.; Liu, D.; Li, H.; Yang, X.; She, Y.; Lei, Y.; Yuan, S. Porous nitrogen-rich g-C<sub>3</sub>N<sub>4</sub> nanotubes for efficient photocatalytic CO<sub>2</sub> reduction. *Appl. Catal. B* **2019**, *256*, 117854. [[CrossRef](#)]
52. Di, J.; Zhu, C.; Ji, M.; Duan, M.; Long, R.; Yan, C.; Gu, K.; Xiong, J.; She, Y.; Xia, J. Defect-Rich Bi<sub>12</sub>O<sub>17</sub>Cl<sub>2</sub> Nanotubes Self-Accelerating Charge Separation for Boosting Photocatalytic CO<sub>2</sub> Reduction. *Angew. Chem. Int. Ed.* **2018**, *57*, 14847–14851. [[CrossRef](#)]
53. Di, J.; Song, P.; Zhu, C.; Chen, C.; Xiong, J.; Duan, M.; Long, R.; Zhou, W.; Xu, M.; Kang, L. Strain-Engineering of Bi<sub>12</sub>O<sub>17</sub>Br<sub>2</sub> Nanotubes for Boosting Photocatalytic CO<sub>2</sub> Reduction. *ACS Mater. Lett.* **2020**, *2*, 1025–1032. [[CrossRef](#)]

54. Xu, G.; Zhang, H.; Wei, J.; Zhang, H.-X.; Wu, X.; Li, Y.; Li, C.; Zhang, J.; Ye, J. Integrating the g-C<sub>3</sub>N<sub>4</sub> Nanosheet with B–H bonding decorated metal–organic framework for CO<sub>2</sub> activation and photoreduction. *ACS Nano* **2018**, *12*, 5333–5340. [[CrossRef](#)] [[PubMed](#)]
55. Xia, P.; Zhu, B.; Yu, J.; Cao, S.; Jaroniec, M. Ultra-thin nanosheet assemblies of graphitic carbon nitride for enhanced photocatalytic CO<sub>2</sub> reduction. *J. Mater. Chem. A* **2017**, *5*, 3230–3238. [[CrossRef](#)]
56. Han, C.; Wang, B.; Wu, C.; Shen, S.; Zhang, X.; Sun, L.; Tian, Q.; Lei, Y.; Wang, Y. Ultrathin SiC nanosheets with high reduction potential for improved CH<sub>4</sub> generation from photocatalytic reduction of CO<sub>2</sub>. *ChemistrySelect* **2019**, *4*, 2211–2217. [[CrossRef](#)]
57. Di, J.; Zhao, X.; Lian, C.; Ji, M.; Xia, J.; Xiong, J.; Zhou, W.; Cao, X.; She, Y.; Liu, H. Atomically-thin Bi<sub>2</sub>MoO<sub>6</sub> nanosheets with vacancy pairs for improved photocatalytic CO<sub>2</sub> reduction. *Nano Energy* **2019**, *61*, 54–59. [[CrossRef](#)]
58. Dai, W.; Yu, J.; Luo, S.; Hu, X.; Yang, L.; Zhang, S.; Li, B.; Luo, X.; Zou, J. WS<sub>2</sub> quantum dots seeding in Bi<sub>2</sub>S<sub>3</sub> nanotubes: A novel Vis-NIR light sensitive photocatalyst with low-resistance junction interface for CO<sub>2</sub> reduction. *Chem. Eng. J.* **2020**, *389*, 123430. [[CrossRef](#)]
59. Zeng, Z.; Yan, Y.; Chen, J.; Zan, P.; Tian, Q.; Chen, P. Boosting the photocatalytic ability of Cu<sub>2</sub>O nanowires for CO<sub>2</sub> conversion by MXene quantum dots. *Adv. Funct. Mater.* **2019**, *29*, 1806500. [[CrossRef](#)]
60. Xie, Z.; Xu, Y.; Li, D.; Chen, L.; Meng, S.; Jiang, D.; Chen, M. Construction of CuO quantum Dots/WO<sub>3</sub> nanosheets 0D/2D Z-scheme heterojunction with enhanced photocatalytic CO<sub>2</sub> reduction activity under visible-light. *J. Alloys Compd.* **2021**, *858*, 157668. [[CrossRef](#)]
61. Ong, W.-J.; Putri, L.K.; Tan, Y.-C.; Tan, L.-L.; Li, N.; Ng, Y.H.; Wen, X.; Chai, S.-P. Unravelling charge carrier dynamics in protonated g-C<sub>3</sub>N<sub>4</sub> interfaced with carbon nanodots as co-catalysts toward enhanced photocatalytic CO<sub>2</sub> reduction: A combined experimental and first-principles DFT study. *Nano Res.* **2017**, *10*, 1673–1696. [[CrossRef](#)]
62. Shi, H.; Long, S.; Hu, S.; Hou, J.; Ni, W.; Song, C.; Li, K.; Gurzadyan, G.G.; Guo, X. Interfacial charge transfer in 0D/2D defect-rich heterostructures for efficient solar-driven CO<sub>2</sub> reduction. *Appl. Catal. B* **2019**, *245*, 760–769. [[CrossRef](#)]
63. Wang, R.; Shen, J.; Sun, K.; Tang, H.; Liu, Q. Enhancement in photocatalytic activity of CO<sub>2</sub> reduction to CH<sub>4</sub> by 0D/2D Au/TiO<sub>2</sub> plasmon heterojunction. *Appl. Surf. Sci.* **2019**, *493*, 1142–1149. [[CrossRef](#)]
64. Wang, J.; Wang, J.; Li, N.; Du, X.; Ma, J.; He, C.; Li, Z. Direct Z-Scheme 0D/2D Heterojunction of CsPbBr<sub>3</sub> Quantum Dots/Bi<sub>2</sub>WO<sub>6</sub> Nanosheets for Efficient Photocatalytic CO<sub>2</sub> Reduction. *ACS Appl. Mater. Interfaces* **2020**, *12*, 31477–31485. [[CrossRef](#)]
65. Xu, F.; Zhu, B.; Cheng, B.; Yu, J.; Xu, J. 1D/2D TiO<sub>2</sub>/MoS<sub>2</sub> hybrid nanostructures for enhanced photocatalytic CO<sub>2</sub> reduction. *Adv. Opt. Mater.* **2018**, *6*, 1800911. [[CrossRef](#)]
66. Tahir, M.; Tahir, B.; Nawawi, M.; Hussain, M.; Muhammad, A. Cu-NPs embedded 1D/2D CNTs/pCN heterojunction composite towards enhanced and continuous photocatalytic CO<sub>2</sub> reduction to fuels. *Appl. Surf. Sci.* **2019**, *485*, 450–461. [[CrossRef](#)]
67. Bian, J.; Qu, Y.; Zhang, X.; Sun, N.; Tang, D.; Jing, L. Dimension-matched plasmonic Au/TiO<sub>2</sub>/BiVO<sub>4</sub> nanocomposites as efficient wide-visible-light photocatalysts to convert CO<sub>2</sub> and mechanistic insights. *J. Mater. Chem. A* **2018**, *6*, 11838–11845. [[CrossRef](#)]
68. Cao, S.; Shen, B.; Tong, T.; Fu, J.; Yu, J. 2D/2D heterojunction of ultrathin MXene/Bi<sub>2</sub>WO<sub>6</sub> nanosheets for improved photocatalytic CO<sub>2</sub> reduction. *Adv. Funct. Mater.* **2018**, *28*, 1800136. [[CrossRef](#)]
69. Kong, X.Y.; Lee, W.Q.; Mohamed, A.R.; Chai, S.-P. Effective steering of charge flow through synergistic inducing oxygen vacancy defects and pn heterojunctions in 2D/2D surface-engineered Bi<sub>2</sub>WO<sub>6</sub>/BiOI cascade: Towards superior photocatalytic CO<sub>2</sub> reduction activity. *Chem. Eng. J.* **2019**, *372*, 1183–1193. [[CrossRef](#)]
70. Tahir, B.; Tahir, M.; Yunus, M.A.C.; Mohamed, A.R.; Siraj, M.; Fatehmulla, A. 2D/2D Mt/m-CN composite with enriched interface charge transfer for boosting photocatalytic CO<sub>2</sub> hydrogenation by H<sub>2</sub> to CH<sub>4</sub> under visible light. *Appl. Surf. Sci.* **2020**, *520*, 146296. [[CrossRef](#)]
71. She, H.; Zhou, H.; Li, L.; Zhao, Z.; Jiang, M.; Huang, J.; Wang, L.; Wang, Q. Construction of a two-dimensional composite derived from TiO<sub>2</sub> and SnS<sub>2</sub> for enhanced photocatalytic reduction of CO<sub>2</sub> into CH<sub>4</sub>. *ACS Sustain. Chem. Eng.* **2018**, *7*, 650–659. [[CrossRef](#)]
72. Lu, M.; Li, Q.; Zhang, C.; Fan, X.; Li, L.; Dong, Y.; Chen, G.; Shi, H. Remarkable photocatalytic activity enhancement of CO<sub>2</sub> conversion over 2D/2D g-C<sub>3</sub>N<sub>4</sub>/BiVO<sub>4</sub> Z-scheme heterojunction promoted by efficient interfacial charge transfer. *Carbon* **2020**, *160*, 342–352. [[CrossRef](#)]
73. Huo, Y.; Zhang, J.; Wang, Z.; Dai, K.; Pan, C.; Liang, C. Efficient interfacial charge transfer of 2D/2D porous carbon nitride/bismuth oxychloride step-scheme heterojunction for boosted solar-driven CO<sub>2</sub> reduction. *J. Colloid Interface Sci.* **2021**, *585*, 684–693. [[CrossRef](#)]
74. Zhang, R.; Huang, Z.; Li, C.; Zuo, Y.; Zhou, Y. Monolithic g-C<sub>3</sub>N<sub>4</sub>/reduced graphene oxide aerogel with in situ embedding of Pd nanoparticles for hydrogenation of CO<sub>2</sub> to CH<sub>4</sub>. *Appl. Surf. Sci.* **2019**, *475*, 953–960. [[CrossRef](#)]
75. Wang, J.; Xia, T.; Wang, L.; Zheng, X.; Qi, Z.; Gao, C.; Zhu, J.; Li, Z.; Xu, H.; Xiong, Y. Enabling Visible-Light-Driven Selective CO<sub>2</sub> Reduction by Doping Quantum Dots: Trapping Electrons and Suppressing H<sub>2</sub> Evolution. *Angew. Chem. Int. Ed.* **2018**, *57*, 16447–16451. [[CrossRef](#)]
76. Wang, C.; Thompson, R.L.; Ohodnicki, P.; Baltrus, J.; Matranga, C. Size-dependent photocatalytic reduction of CO<sub>2</sub> with PbS quantum dot sensitized TiO<sub>2</sub> heterostructured photocatalysts. *J. Mater. Chem.* **2011**, *21*, 13452–13457. [[CrossRef](#)]
77. Kuehnel, M.F.; Sahm, C.D.; Neri, G.; Lee, J.R.; Orchard, K.L.; Cowan, A.J.; Reiser, E. ZnSe quantum dots modified with a Ni (cyclam) catalyst for efficient visible-light driven CO<sub>2</sub> reduction in water. *Chem. Sci.* **2018**, *9*, 2501–2509. [[CrossRef](#)] [[PubMed](#)]
78. Huang, J.; Gatty, M.G.; Xu, B.; Pati, P.B.; Etman, A.S.; Tian, L.; Sun, J.; Hammarström, L.; Tian, H. Covalently linking CuInS<sub>2</sub> quantum dots with a Re catalyst by click reaction for photocatalytic CO<sub>2</sub> reduction. *Dalton Trans.* **2018**, *47*, 10775–10783. [[CrossRef](#)] [[PubMed](#)]

79. Chen, L.; Zhang, M.; Yang, J.; Li, Y.; Sivalingam, Y.; Shi, Q.; Xie, M.; Han, W. Synthesis of BiVO<sub>4</sub> quantum dots/reduced graphene oxide composites for CO<sub>2</sub> reduction. *Mater. Sci. Semicond. Process.* **2019**, *102*, 104578. [[CrossRef](#)]
80. Qin, H.; Guo, R.-T.; Liu, X.-Y.; Shi, X.; Wang, Z.-Y.; Tang, J.-Y.; Pan, W.-G. 0D NiS<sub>2</sub> quantum dots modified 2D g-C<sub>3</sub>N<sub>4</sub> for efficient photocatalytic CO<sub>2</sub> reduction. *Colloids Surf. A Physicochem. Eng. Asp.* **2020**, *600*, 124912. [[CrossRef](#)]
81. Yadav, D.; Yadav, R.K.; Kumar, A.; Park, N.J.; Baeg, J.O. Functionalized Graphene Quantum Dots as Efficient Visible-Light Photocatalysts for Selective Solar Fuel Production from CO<sub>2</sub>. *ChemCatChem* **2016**, *8*, 3389–3393. [[CrossRef](#)]
82. Han, C.; Li, J.; Ma, Z.; Xie, H.; Waterhouse, G.I.; Ye, L.; Zhang, T. Black phosphorus quantum dot/g-C<sub>3</sub>N<sub>4</sub> composites for enhanced CO<sub>2</sub> photoreduction to CO. *Sci. China Mater.* **2018**, *61*, 1159–1166. [[CrossRef](#)]
83. Guo, R.-T.; Liu, X.-Y.; Qin, H.; Wang, Z.-Y.; Shi, X.; Pan, W.-G.; Fu, Z.-G.; Tang, J.-Y.; Jia, P.-Y.; Miao, Y.-F. Photocatalytic reduction of CO<sub>2</sub> into CO over nanostructure Bi<sub>2</sub>S<sub>3</sub> quantum dots/g-C<sub>3</sub>N<sub>4</sub> composites with Z-scheme mechanism. *Appl. Surf. Sci.* **2020**, *500*, 144059. [[CrossRef](#)]
84. Sharma, S.; Dutta, V.; Singh, P.; Raizada, P.; Rahmani-Sani, A.; Hosseini-Bandegharaei, A.; Thakur, V.K. Carbon quantum dot supported semiconductor photocatalysts for efficient degradation of organic pollutants in water: A review. *J. Clean. Prod.* **2019**, *228*, 755–769. [[CrossRef](#)]
85. Fernando, K.S.; Sahu, S.; Liu, Y.; Lewis, W.K.; Gulians, E.A.; Jafariyan, A.; Wang, P.; Bunker, C.E.; Sun, Y.-P. Carbon quantum dots and applications in photocatalytic energy conversion. *ACS Appl. Mater. Interfaces* **2015**, *7*, 8363–8376. [[CrossRef](#)] [[PubMed](#)]
86. Wang, X.; Feng, Y.; Dong, P.; Huang, J. A mini review on carbon quantum dots: Preparation, properties, and electrocatalytic application. *Front. Chem.* **2019**, *7*, 671. [[CrossRef](#)]
87. Li, Q.; Wang, S.; Sun, Z.; Tang, Q.; Liu, Y.; Wang, L.; Wang, H.; Wu, Z. Enhanced CH<sub>4</sub> selectivity in CO<sub>2</sub> photocatalytic reduction over carbon quantum dots decorated and oxygen doping g-C<sub>3</sub>N<sub>4</sub>. *Nano Res.* **2019**, *12*, 2749–2759. [[CrossRef](#)]
88. Zeng, Z.; Chen, S.; Tan, T.T.Y.; Xiao, F.-X. Graphene quantum dots (GQDs) and its derivatives for multifarious photocatalysis and photoelectrocatalysis. *Catal. Today* **2018**, *315*, 171–183. [[CrossRef](#)]
89. Kim, S.Y.; Jang, H.W. Lead-free all-inorganic halide perovskite quantum dots: Review and outlook. *J. Korean Ceram. Soc.* **2020**, *57*, 455–479.
90. Moon, H.; Lee, C.; Lee, W.; Kim, J.; Chae, H. Stability of quantum dots, quantum dot films, and quantum dot light-emitting diodes for display applications. *Adv. Mater.* **2019**, *31*, 1804294. [[CrossRef](#)]
91. Lee, H.; Horn, M.W. Sculptured platinum nanowire counter electrodes for dye-sensitized solar cells. *Thin Solid Film.* **2013**, *540*, 208–211. [[CrossRef](#)]
92. Lee, H.; In, S.; Horn, M.W. Plasmonic enhancement of CO<sub>2</sub> conversion to methane using sculptured copper thin films grown directly on TiO<sub>2</sub>. *Thin Solid Films* **2014**, *565*, 105–110. [[CrossRef](#)]
93. Xiao, F.X.; Miao, J.; Tao, H.B.; Hung, S.F.; Wang, H.Y.; Yang, H.B.; Chen, J.; Chen, R.; Liu, B. One-dimensional hybrid nanostructures for heterogeneous photocatalysis and photoelectrocatalysis. *Small* **2015**, *11*, 2115–2131. [[CrossRef](#)] [[PubMed](#)]
94. Sui, Y.; Su, C.; Yang, X.; Hu, J.; Lin, X. Ag-AgBr nanoparticles loaded on TiO<sub>2</sub> nanofibers as an efficient heterostructured photocatalyst driven by visible light. *J. Mol. Catal. A Chem.* **2015**, *410*, 226–234. [[CrossRef](#)]
95. Wang, M.; Pang, X.; Zheng, D.; He, Y.; Sun, L.; Lin, C.; Lin, Z. Nonepitaxial growth of uniform and precisely size-tunable core/shell nanoparticles and their enhanced plasmon-driven photocatalysis. *J. Mater. Chem. A* **2016**, *4*, 7190–7199. [[CrossRef](#)]
96. Nasr, M.; Eid, C.; Habchi, R.; Miele, P.; Bechelany, M. Recent progress on titanium dioxide nanomaterials for photocatalytic applications. *ChemSusChem* **2018**, *11*, 3023–3047. [[CrossRef](#)] [[PubMed](#)]
97. Chen, X.; Mao, S.S. Titanium dioxide nanomaterials: Synthesis, properties, modifications, and applications. *Chem. Rev.* **2007**, *107*, 2891–2959. [[CrossRef](#)] [[PubMed](#)]
98. Fujishima, A.; Zhang, X.; Tryk, D.A. TiO<sub>2</sub> photocatalysis and related surface phenomena. *Surf. Sci. Rep.* **2008**, *63*, 515–582. [[CrossRef](#)]
99. Kar, P.; Zeng, S.; Zhang, Y.; Vahidzadeh, E.; Manuel, A.; Kisslinger, R.; Alam, K.M.; Thakur, U.K.; Mahdi, N.; Kumar, P. High rate CO<sub>2</sub> photoreduction using flame annealed TiO<sub>2</sub> nanotubes. *Appl. Catal. B* **2019**, *243*, 522–536. [[CrossRef](#)]
100. Wu, J.; Feng, Y.; Li, D.; Han, X.; Liu, J. Efficient photocatalytic CO<sub>2</sub> reduction by P–O linked g-C<sub>3</sub>N<sub>4</sub>/TiO<sub>2</sub>-nanotubes Z-scheme composites. *Energy* **2019**, *178*, 168–175. [[CrossRef](#)]
101. Rambabu, Y.; Kumar, U.; Singhal, N.; Kaushal, M.; Jaiswal, M.; Jain, S.L.; Roy, S.C. Photocatalytic reduction of carbon dioxide using graphene oxide wrapped TiO<sub>2</sub> nanotubes. *Appl. Surf. Sci.* **2019**, *485*, 48–55. [[CrossRef](#)]
102. Zhao, H.; Chen, J.; Rao, G.; Deng, W.; Li, Y. Enhancing photocatalytic CO<sub>2</sub> reduction by coating an ultrathin Al<sub>2</sub>O<sub>3</sub> layer on oxygen deficient TiO<sub>2</sub> nanorods through atomic layer deposition. *Appl. Surf. Sci.* **2017**, *404*, 49–56. [[CrossRef](#)]
103. Wang, X.; Zhang, Z.; Huang, Z.; Dong, P.; Nie, X.; Jin, Z.; Zhang, X. Synergistic effect of N-Ho on photocatalytic CO<sub>2</sub> reduction for N/Ho co-doped TiO<sub>2</sub> nanorods. *Mater. Res. Bull.* **2019**, *118*, 110502. [[CrossRef](#)]
104. Ohno, T.; Higo, T.; Murakami, N.; Saito, H.; Zhang, Q.; Yang, Y.; Tsubota, T. Photocatalytic reduction of CO<sub>2</sub> over exposed-crystal-face-controlled TiO<sub>2</sub> nanorod having a brookite phase with co-catalyst loading. *Appl. Catal. B* **2014**, *152*, 309–316. [[CrossRef](#)]
105. Tahir, M.; Tahir, B.; Amin, N.A.S. Gold-nanoparticle-modified TiO<sub>2</sub> nanowires for plasmon-enhanced photocatalytic CO<sub>2</sub> reduction with H<sub>2</sub> under visible light irradiation. *Appl. Surf. Sci.* **2015**, *356*, 1289–1299. [[CrossRef](#)]
106. Shen, M.; Zhang, L.; Shi, J. Converting CO<sub>2</sub> into fuels by graphitic carbon nitride-based photocatalysts. *Nanotechnology* **2018**, *29*, 412001. [[CrossRef](#)] [[PubMed](#)]

107. Akhundi, A.; Habibi-Yangjeh, A.; Abitorabi, M.; Rahim Pourn, S. Review on photocatalytic conversion of carbon dioxide to value-added compounds and renewable fuels by graphitic carbon nitride-based photocatalysts. *Catal. Rev.* **2019**, *61*, 595–628. [[CrossRef](#)]
108. Bakar, S.A.; Ribeiro, C. Nitrogen-doped titanium dioxide: An overview of material design and dimensionality effect over modern applications. *J. Photochem. Photobiol. C* **2016**, *27*, 1–29. [[CrossRef](#)]
109. Narita, A.; Wang, X.-Y.; Feng, X.; Müllen, K. New advances in nanographene chemistry. *Chem. Soc. Rev.* **2015**, *44*, 6616–6643. [[CrossRef](#)]
110. Khan, B.; Raziq, F.; Faheem, M.B.; Farooq, M.U.; Hussain, S.; Ali, F.; Ullah, A.; Mavlonov, A.; Zhao, Y.; Liu, Z. Electronic and nanostructure engineering of bifunctional MoS<sub>2</sub> towards exceptional visible-light photocatalytic CO<sub>2</sub> reduction and pollutant degradation. *J. Hazard. Mater.* **2020**, *381*, 120972. [[CrossRef](#)]
111. Wang, X.; He, J.; Mao, L.; Cai, X.; Sun, C.; Zhu, M. CsPbBr<sub>3</sub> perovskite nanocrystals anchoring on monolayer MoS<sub>2</sub> nanosheets for efficient photocatalytic CO<sub>2</sub> reduction. *Chem. Eng. J.* **2020**, 128077. [[CrossRef](#)]
112. Wang, J.; Li, L.; Wang, L.; Liu, Y.; Sun, W.; Li, W.; Li, G. In situ growth of MoS<sub>2</sub> nanosheet arrays and TS<sub>2</sub> (T = Fe, Co, and Ni) nanocubes onto molybdate for efficient oxygen evolution reaction and improved hydrogen evolution reaction. *ACS Omega* **2018**, *3*, 464–471. [[CrossRef](#)]
113. He, J.; Chen, L.; Yi, Z.-Q.; Au, C.-T.; Yin, S.-F. CdS nanorods coupled with WS<sub>2</sub> nanosheets for enhanced photocatalytic hydrogen evolution activity. *Ind. Eng. Chem. Res.* **2016**, *55*, 8327–8333. [[CrossRef](#)]
114. Cao, Y.; Zhang, R.; Zhou, T.; Jin, S.; Huang, J.; Ye, L.; Huang, Z.; Wang, F.; Zhou, Y. B–O Bonds in Ultrathin Boron Nitride Nanosheets to Promote Photocatalytic Carbon Dioxide Conversion. *ACS Appl. Mater. Interfaces* **2020**, *12*, 9935–9943. [[CrossRef](#)] [[PubMed](#)]
115. Ali, W.; Zhang, X.; Zhang, X.; Ali, S.; Zhao, L.; Shaheen, S.; Jing, L. Improved visible-light activities of g-C<sub>3</sub>N<sub>4</sub> nanosheets by co-modifying nano-sized SnO<sub>2</sub> and Ag for CO<sub>2</sub> reduction and 2, 4-dichlorophenol degradation. *Mater. Res. Bull.* **2020**, *122*, 110676. [[CrossRef](#)]
116. Wang, X.; He, J.; Li, J.; Lu, G.; Dong, F.; Majima, T.; Zhu, M. Immobilizing perovskite CsPbBr<sub>3</sub> nanocrystals on Black phosphorus nanosheets for boosting charge separation and photocatalytic CO<sub>2</sub> reduction. *Appl. Catal. B* **2020**, *277*, 119230. [[CrossRef](#)]
117. Li, J.; Liu, P.; Huang, H.; Li, Y.; Tang, Y.; Mei, D.; Zhong, C. Metal-free 2D/2D black phosphorus and covalent triazine framework heterostructure for CO<sub>2</sub> photoreduction. *ACS Sustain. Chem. Eng.* **2020**, *8*, 5175–5183. [[CrossRef](#)]
118. Zhu, X.; Huang, S.; Yu, Q.; She, Y.; Yang, J.; Zhou, G.; Li, Q.; She, X.; Deng, J.; Li, H. In-situ hydroxyl modification of monolayer black phosphorus for stable photocatalytic carbon dioxide conversion. *Appl. Catal. B* **2020**, *269*, 118760. [[CrossRef](#)]
119. Wei, Z.-H.; Wang, Y.-F.; Li, Y.-Y.; Zhang, L.; Yao, H.-C.; Li, Z.-J. Enhanced photocatalytic CO<sub>2</sub> reduction activity of Z-scheme CdS/BiVO<sub>4</sub> nanocomposite with thinner BiVO<sub>4</sub> nanosheets. *J. CO<sub>2</sub> Util.* **2018**, *28*, 15–25. [[CrossRef](#)]
120. Ma, Z.; Li, P.; Ye, L.; Zhou, Y.; Su, F.; Ding, C.; Xie, H.; Bai, Y.; Wong, P.K. Oxygen vacancies induced exciton dissociation of flexible BiOCl nanosheets for effective photocatalytic CO<sub>2</sub> conversion. *J. Mater. Chem. A* **2017**, *5*, 24995–25004. [[CrossRef](#)]
121. Ye, L.; Jin, X.; Liu, C.; Ding, C.; Xie, H.; Chu, K.H.; Wong, P.K. Thickness-ultrathin and bismuth-rich strategies for BiOBr to enhance photoreduction of CO<sub>2</sub> into solar fuels. *Appl. Catal. B* **2016**, *187*, 281–290. [[CrossRef](#)]
122. Vu, N.N.; Nguyen, C.C.; Kaliaguine, S.; Do, T.O. Reduced Cu/Pt–HCa<sub>2</sub>Ta<sub>3</sub>O<sub>10</sub> Perovskite Nanosheets for Sunlight-Driven Conversion of CO<sub>2</sub> into Valuable Fuels. *Adv. Sustain. Syst.* **2017**, *1*, 1700048. [[CrossRef](#)]
123. Pan, A.; Ma, X.; Huang, S.; Wu, Y.; Jia, M.; Shi, Y.; Liu, Y.; Wangyang, P.; He, L.; Liu, Y. CsPbBr<sub>3</sub> perovskite nanocrystal grown on MXene nanosheets for enhanced photoelectric detection and photocatalytic CO<sub>2</sub> reduction. *J. Phys. Chem. Lett.* **2019**, *10*, 6590–6597. [[CrossRef](#)] [[PubMed](#)]
124. Xie, J.; Li, S.; Wang, R.; Zhang, H.; Xie, Y. Grain boundary engineering in atomically-thin nanosheets achieving bright white light emission. *Chem. Sci.* **2014**, *5*, 1328–1335. [[CrossRef](#)]
125. Liu, Q.; Wu, D.; Zhou, Y.; Su, H.; Wang, R.; Zhang, C.; Yan, S.; Xiao, M.; Zou, Z. Single-crystalline, ultrathin ZnGa<sub>2</sub>O<sub>4</sub> nanosheet scaffolds to promote photocatalytic activity in CO<sub>2</sub> reduction into methane. *ACS Appl. Mater. Interfaces* **2014**, *6*, 2356–2361. [[CrossRef](#)] [[PubMed](#)]
126. Li, J.; Zhang, M.; Guan, Z.; Li, Q.; He, C.; Yang, J. Synergistic effect of surface and bulk single-electron-trapped oxygen vacancy of TiO<sub>2</sub> in the photocatalytic reduction of CO<sub>2</sub>. *Appl. Catal. B* **2017**, *206*, 300–307. [[CrossRef](#)]
127. Liang, M.; Borjigin, T.; Zhang, Y.; Liu, B.; Liu, H.; Guo, H. Controlled assemble of hollow heterostructured g-C<sub>3</sub>N<sub>4</sub>@CeO<sub>2</sub> with rich oxygen vacancies for enhanced photocatalytic CO<sub>2</sub> reduction. *Appl. Catal. B* **2019**, *243*, 566–575. [[CrossRef](#)]
128. He, Y.; Rao, H.; Song, K.; Li, J.; Yu, Y.; Lou, Y.; Li, C.; Han, Y.; Shi, Z.; Feng, S. 3D hierarchical ZnIn<sub>2</sub>S<sub>4</sub> nanosheets with rich Zn vacancies boosting photocatalytic CO<sub>2</sub> reduction. *Adv. Funct. Mater.* **2019**, *29*, 1905153. [[CrossRef](#)]
129. Fu, J.; Bao, H.; Liu, Y.; Mi, Y.; Qiu, Y.; Zhuo, L.; Liu, X.; Luo, J. Oxygen Doping Induced by Nitrogen Vacancies in Nb<sub>4</sub>N<sub>5</sub> Enables Highly Selective CO<sub>2</sub> Reduction. *Small* **2020**, *16*, 1905825.
130. Di, J.; Chen, C.; Zhu, C.; Song, P.; Xiong, J.; Ji, M.; Zhou, J.; Fu, Q.; Xu, M.; Hao, W. Bismuth vacancy-tuned bismuth oxybromide ultrathin nanosheets toward photocatalytic CO<sub>2</sub> reduction. *ACS Appl. Mater. Interfaces* **2019**, *11*, 30786–30792. [[CrossRef](#)]
131. Li, H.; Zhang, L. Photocatalytic performance of different exposed crystal facets of BiOCl. *Curr. Opin. Green Sustain. Chem.* **2017**, *6*, 48–56. [[CrossRef](#)]
132. Yao, Y.-C.; Dai, X.-R.; Hu, X.-Y.; Huang, S.-Z.; Jin, Z. Synthesis of Ag-decorated porous TiO<sub>2</sub> nanowires through a sunlight induced reduction method and its enhanced photocatalytic activity. *Appl. Surf. Sci.* **2016**, *387*, 469–476. [[CrossRef](#)]

133. Wei, Z.; Rosa, L.; Wang, K.; Endo, M.; Juodkazis, S.; Ohtani, B.; Kowalska, E. Size-controlled gold nanoparticles on octahedral anatase particles as efficient plasmonic photocatalyst. *Appl. Catal. B* **2017**, *206*, 393–405. [[CrossRef](#)] [[PubMed](#)]
134. Schaadt, D.; Feng, B.; Yu, E. Enhanced semiconductor optical absorption via surface plasmon excitation in metal nanoparticles. *Appl. Phys. Lett.* **2005**, *86*, 063106. [[CrossRef](#)]
135. Kim, K.-H.; Husakou, A.; Herrmann, J. Linear and nonlinear optical characteristics of composites containing metal nanoparticles with different sizes and shapes. *Opt. Express* **2010**, *18*, 7488–7496. [[CrossRef](#)]
136. Xu, F.; Meng, K.; Cheng, B.; Yu, J.; Ho, W. Enhanced Photocatalytic Activity and Selectivity for CO<sub>2</sub> Reduction over a TiO<sub>2</sub> Nanofibre Mat Using Ag and MgO as Bi-Cocatalyst. *ChemCatChem* **2019**, *11*, 465–472. [[CrossRef](#)]
137. Lu, C.; Li, J.; Yan, J.; Li, B.; Huang, B.; Lou, Z. Surface plasmon resonance and defects on tungsten oxides synergistically boost high-selective CO<sub>2</sub> reduction for ethylene. *Appl. Mater. Today* **2020**, *20*, 100744. [[CrossRef](#)]
138. Kamat, P.V. Photophysical, photochemical and photocatalytic aspects of metal nanoparticles. *J. Phys. Chem. B* **2002**, *106*, 7729–7744. [[CrossRef](#)]
139. Rheinberger, T.; Ohm, D.; Zhumaev, U.E.; Domke, K.F. Extending surface plasmon resonance spectroscopy to platinum surfaces. *Electrochim. Acta* **2019**, *314*, 96–101. [[CrossRef](#)]
140. Zhao, H.; Zheng, X.; Feng, X.; Li, Y. CO<sub>2</sub> reduction by plasmonic Au nanoparticle-decorated TiO<sub>2</sub> photocatalyst with an ultrathin Al<sub>2</sub>O<sub>3</sub> Interlayer. *J. Phys. Chem. C* **2018**, *122*, 18949–18956. [[CrossRef](#)]
141. Low, J.; Qiu, S.; Xu, D.; Jiang, C.; Cheng, B. Direct evidence and enhancement of surface plasmon resonance effect on Ag-loaded TiO<sub>2</sub> nanotube arrays for photocatalytic CO<sub>2</sub> reduction. *Appl. Surf. Sci.* **2018**, *434*, 423–432. [[CrossRef](#)]
142. He, Z.; Zhang, J.; Li, X.; Guan, S.; Dai, M.; Wang, S. 1D/2D Heterostructured Photocatalysts: From Design and Unique Properties to Their Environmental Applications. *Small* **2020**, *16*, 2005051. [[CrossRef](#)]
143. Li, B.; Cao, Z.; Wang, S.; Wei, Q.; Shen, Z. BiVO<sub>4</sub> quantum dot-decorated BiPO<sub>4</sub> nanorods 0D/1D heterojunction for enhanced visible-light-driven photocatalysis. *Dalton Trans.* **2018**, *47*, 10288–10298. [[CrossRef](#)]
144. Jo, W.-K.; Kumar, S.; Eslava, S.; Tonda, S. Construction of Bi<sub>2</sub>WO<sub>6</sub>/RGO/g-C<sub>3</sub>N<sub>4</sub> 2D/2D/2D hybrid Z-scheme heterojunctions with large interfacial contact area for efficient charge separation and high-performance photoreduction of CO<sub>2</sub> and H<sub>2</sub>O into solar fuels. *Appl. Catal. B* **2018**, *239*, 586–598. [[CrossRef](#)]
145. He, F.; Zhu, B.; Cheng, B.; Yu, J.; Ho, W.; Macyk, W. 2D/2D/0D TiO<sub>2</sub>/C<sub>3</sub>N<sub>4</sub>/Ti<sub>3</sub>C<sub>2</sub> MXene composite S-scheme photocatalyst with enhanced CO<sub>2</sub> reduction activity. *Appl. Catal. B* **2020**, *272*, 119006. [[CrossRef](#)]
146. Fu, J.; Zhu, B.; Jiang, C.; Cheng, B.; You, W.; Yu, J. Hierarchical porous O-doped g-C<sub>3</sub>N<sub>4</sub> with enhanced photocatalytic CO<sub>2</sub> reduction activity. *Small* **2017**, *13*, 1603938. [[CrossRef](#)] [[PubMed](#)]
147. Gao, J.; Shen, Q.; Guan, R.; Xue, J.; Liu, X.; Jia, H.; Li, Q.; Wu, Y. Oxygen vacancy self-doped black TiO<sub>2</sub> nanotube arrays by aluminothermic reduction for photocatalytic CO<sub>2</sub> reduction under visible light illumination. *J. CO<sub>2</sub> Util.* **2020**, *35*, 205–215. [[CrossRef](#)]
148. Xiu, Z.; Guo, M.; Zhao, T.; Pan, K.; Xing, Z.; Li, Z.; Zhou, W. Recent advances in Ti<sup>3+</sup> self-doped nanostructured TiO<sub>2</sub> visible light photocatalysts for environmental and energy applications. *Chem. Eng. J.* **2020**, *382*, 123011. [[CrossRef](#)]
149. Wang, H.; Liu, X.; Niu, P.; Wang, S.; Shi, J.; Li, L. Porous two-dimensional materials for photocatalytic and electrocatalytic applications. *Matter* **2020**, *2*, 1377–1413. [[CrossRef](#)]
150. Tian, N.; Xiao, K.; Zhang, Y.; Lu, X.; Ye, L.; Gao, P.; Ma, T.; Huang, H. Reactive sites rich porous tubular yolk-shell g-C<sub>3</sub>N<sub>4</sub> via precursor recrystallization mediated microstructure engineering for photoreduction. *Appl. Catal. B* **2019**, *253*, 196–205. [[CrossRef](#)]